Space environment of an asteroid preserved on micrograins returned by the Hayabusa spacecraft

Eizo Nakamura[a,1], Akio Makishima[a], Takuya Moriguti[a], Katsura Kobayashi[a], Ryoji Tanaka[a], Tak Kunihiro[a], Tatsuki Tsujimori[a], Chie Sakaguchi[a], Hiroshi Kitagawa[a], Tsutomu Ota[a], Yusuke Yachi[a], Toru Yada[b], Masanao Abe[b], Akio Fujimura[b], Munetaka Ueno[b], Toshifumi Mukai[b], Makoto Yoshikawa[b], and Jun'ichiro Kawaguchi[b]

[a]The Pheasant Memorial Laboratory for Geochemistry and Cosmochemistry, Institute for Study of the Earth's Interior, Okayama University, Misasa, Tottori 682-0193, Japan; and [b]Japan Aerospace Exploration Agency, Yoshinodai 3-1-1, Chuo, Sagamihara, Kanagawa 252-5210, Japan

Edited by* Ikuo Kushiro, University of Tokyo, Tokyo, Japan, and approved January 28, 2012 (received for review October 4, 2011)

Records of micrometeorite collisions at down to submicron scales were discovered on dust grains recovered from near-Earth asteroid 25143 (Itokawa). Because the grains were sampled from very near the surface of the asteroid, by the Hayabusa spacecraft, their surfaces reflect the low-gravity space environment influencing the physical nature of the asteroid exterior. The space environment was examined by description of grain surfaces and asteroidal scenes were reconstructed. Chemical and O isotope compositions of five lithic grains, with diameters near 50 μm, indicate that the uppermost layer of the rubble-pile-textured Itokawa is largely composed of equilibrated LL-ordinary-chondrite-like material with superimposed effects of collisions. The surfaces of the grains are dominated by fractures, and the fracture planes contain not only sub-μm-sized craters but also a large number of sub-μm- to several-μm-sized adhered particles, some of the latter composed of glass. The size distribution and chemical compositions of the adhered particles, together with the occurrences of the sub-μm-sized craters, suggest formation by hypervelocity collisions of micrometeorites at down to nm scales, a process expected in the physically hostile environment at an asteroid's surface. We describe impact-related phenomena, ranging in scale from 10^{-9} to 10^{4} meters, demonstrating the central role played by impact processes in the long-term evolution of planetary bodies. Impact appears to be an important process shaping the exteriors of not only large planetary bodies, such as the moon, but also low-gravity bodies such as asteroids.

impacts | sample-return mission | interplanetary dust | space weathering | comprehensive analysis

Solar bodies have evolved from dust to planets with interactions between dust and debris, and asteroids are considered intermediate products of this evolution. Asteroids were not melted and retain their primitive morphology and geochemistry, thus allowing us to investigate interactions between solids and the solar nebula. Meteorites are regarded as fragments of asteroids that fall to Earth's surface. However, information regarding the outer surface of asteroids is presumably destroyed during atmospheric entry, preventing examination of solar space-exposed exteriors of planetary bodies other than that of the moon sampled by the Apollo missions. Nearly all the materials now residing in the planets were processed through high-velocity impacts; however, previous investigation of collisional processes on low-gravity solar bodies has been limited to remote observations by satellites, with no direct sampling of such bodies.

The Japan Aerospace Exploration Agency (JAXA) conducted the Hayabusa mission with the goal of better understanding solar system evolution through direct sampling of an asteroid and return of the samples to Earth for detailed analytical work. A target was set to the near-Earth asteroid 25143 Itokawa, an example of a spectral type-S asteroid common in the inner part of the asteroid belt. On-site observations by the spacecraft showed that Itokawa is $550 \times 298 \times 224$ m in size and has rubble-pile structure with a density of 1.9 g/cm^3 and an escape velocity of 0.2 m/s (1). An onboard multiband camera (AMICA) imaged the solid exterior of the asteroid and revealed a diversity of surface morphologies (2, 3). Based on topography and spectroscopic observations, a sampling location on a smooth terrain called Muses Sea was selected.

The original plan of the mission was to collect rocks from Itokawa's surface by an impact sampling method. However, at the time of the touchdown, no projectile was fired (4), resulting in only minimal sample recovery. Collection of material from very near the surface resulted from gentle flicking by the tip of the sampler horn. The sample capsule was returned to Earth on June 13, 2010, and opened at a JAXA curation facility. As a part of the mission, initial analyses of returned grains were carried out by several teams of researchers. One team reported on the general properties of the grains and concluded that the building blocks of the rubble pile were identical to those of equilibrated LL-ordinary chondrites with mild overprinting by "space weathering" (5–8). This conclusion is consistent with the spectroscopic observations made from Earth and by the Hayabusa spacecraft (9, 10); however, some key questions remain. What record of the environment at the asteroid exterior exists on the surface of grains deposited there and, more broadly, what were the most important processes shaping the postaccretion appearance of this asteroid? Nanometer-scale investigation of the surfaces of these micrograins can help us characterize the space environment of this and other asteroids, an important step toward more general understanding of impact phenomena in the inner solar system.

In this paper, we summarize the results of our comprehensive initial analysis of the sizes, morphology, mineralogy, and geochemistry of five lithic grains from Itokawa. We in particular focus on grain surfaces and report discoveries of (*i*) craters with diameters of 100–200 nm that provide direct evidence of sub-μm-scale bombardment at the asteroid surface, and (*ii*) objects adhered to the surfaces of these grains and representing high-velocity impacts. We suggest that the space environment alters asteroid surfaces by a combination of disaggregation, cratering, melting, adhesion, agglutination, and implantation/sputtering, all consequences of constant bombardment by nm- to μm-scale particles. Our observations regarding the sub-μm-scale physical

Author contributions: E.N. undertook the initial analysis; A.M. and T. Moriguti prepared reference materials; K.K. coordinated the flow of the analytical work through the laboratories and performed the FIB slabbing of the grains; R.T. analyzed oxygen isotopes for the reference materials; T.K. carried out in situ oxygen-isotope analyses; T.T. carried out petrographic and mineralogical investigations; C.S. evaluated adhered objects; H.K. assisted in the electron and ion probe work; T.O. determined elemental compositions; Y.Y. documented the sample status; T.Y., M.A., A.F., M.U., T. Mukai, M.Y., and J.K. worked on sample preparation; and E.N., A.M., T. Moriguti, K.K., R.T., T.K., and T.T. wrote the paper.

The authors declare no conflict of interest.

*This Direct Submission article had a prearranged editor.

Freely available online through the PNAS open access option.

[1]To whom correspondence should be addressed. E-mail: eizonak@misasa.okayama-u.ac.jp.

See Author Summary on page 4031 (volume 109, number 11).

This article contains supporting information online at www.pnas.org/lookup/suppl/doi:10.1073/pnas.1116236109/-/DCSupplemental.

and chemical changes on these grain surfaces help elucidate the process of space weathering that, at larger scales at an asteroid surface, produces a reddening and a reduction in band depth in spectroscopic observations.

Results

Mineralogical Properties of the Five Grains. The grains we investigated were 40–110 μm-sized, mono- or poly-phase fragments. Grains A–E surveyed in this study have JAXA-ID RA-QD02-0121, 0093, 0095, 0118, and 0116, respectively. All grains exhibit angular outlines and high surface relief. Grain A (40 × 30 μm) consists of olivine and low-Ca pyroxene (Fig. 1*A*), with the olivine showing sets of sharply defined lamellae with widths at the sub-μm-scale (Fig. 1*B*). These lamellae could reflect high strain rates and high shear stresses associated with shock compression and have previously been referred to as shock lamellae (11). An object with a ropey fabric, observed on and along a crack crosscutting the lamellae, appears to have originated from melt (Fig. 1*C*). Grain B (110 × 90 μm) is a fragment of a single olivine (Fig. 2*A*) with inclusions of oriented, very thin (10–20 μm), subparallel plates with the composition of plagioclase. This intergrowth resembles the "barred olivine" observed in chondrules (12) (Fig. 2*B*). A 1 μm-sized diopside is also included in this single olivine grain, and sub-μm-sized chromites are included in both the olivine and the plagioclase. Grain C (70 × 50 μm) consists of diopside and plagioclase (Fig. 3*A*), with minor K-feldspar (Fig. 3*B*). A trail of microbowls crosscuts both the diopside and the plagioclase (Fig. 3*C*). These microbowls are filled with troilite, to varying degrees, perhaps reflecting some evaporation of troilite during thermal metamorphism. The plagioclase exhibits unusually low birefringence (Fig. 3*B*) suggesting that its structure is intermediate between crystalline and glassy. When observed in meteorites, such plagioclase is referred to as being diaplectic and indicative of shock metamorphism at certain impact pressures (13). The plagioclase in Grain C shows a sharp contact with diopside, likely reflecting formation by devitrification of chondrule glass during the thermal metamorphism (14). Grain D is a fragment (50 × 40 μm) of low-Ca pyroxene for which no inclusions or shock-related textures were observed. For Grain E (50 × 40 μm), which also consists of low-Ca pyroxene, only surface observations were undertaken (Fig. 4*A*).

Grains were cut into three pieces, by focused-ion beam methods (FIB), for the electron and ion microprobe analyses (Fig. 3*A*). The middle slabs with two very flat, planar surfaces were used for these analyses and the other pieces were preserved for future work. In situ O isotope analyses were carried out by secondary-ion mass-spectrometry (SIMS) on Grains A–D. The analytical

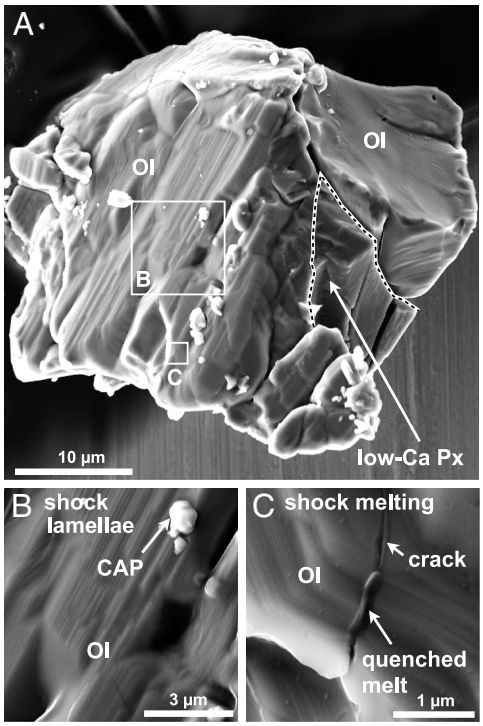

Fig. 1. Surface images obtained by SEM of Grain A with shock-induced textures. (*A*) The entire Grain A, indicating the locations for the higher-magnification images. (*B*) Shock lamellae developed on olivine (Ol). (*C*) Quenched melt on and along a crack crosscutting the shock lamellae.

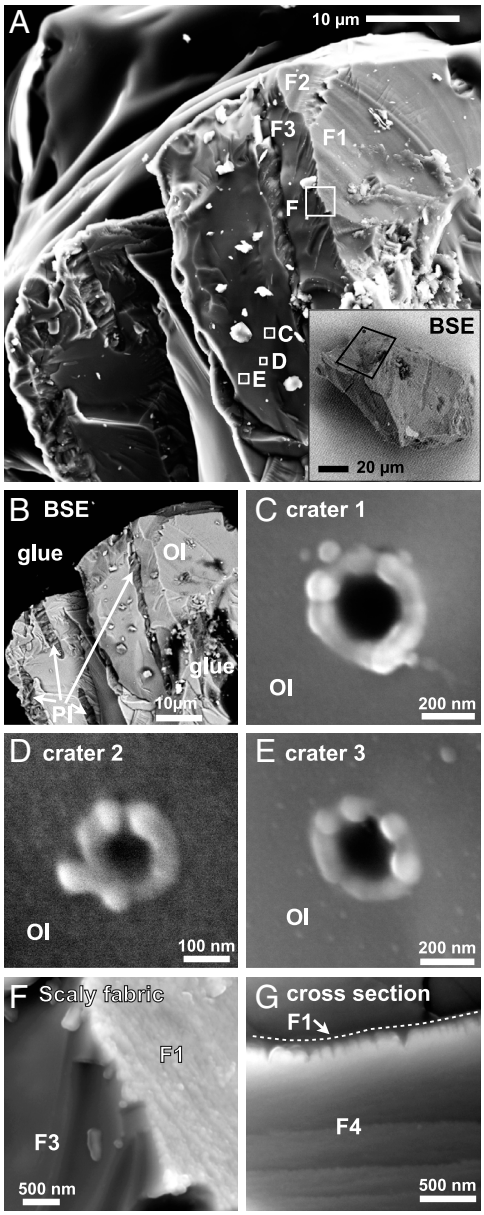

Fig. 2. Surface images (SEM unless otherwise specified) of Grain B with sub-μm-sized craters. (*A*) A part of Grain B, with the location on the complete grain indicated in the inserted BSE (back-scattered electron) image located in the SE part of the photograph. F1, F2, and F3 represent fracture planes, numbered in order of the relative timing of their formation (with F1 the earliest-form plane). (*B*) A BSE image of the region of (*A*), showing a barred-olivine texture. (*C*, *D*, *E*) Sub-μm-sized craters on Ol substrate. A pit rim with chains of seven or eight spheres. (*F*) An intersection of F1 and F3 and a scaly fabric on F1. (*G*) A cross section of the scaly fabric showing the sawtooth morphology on F1.

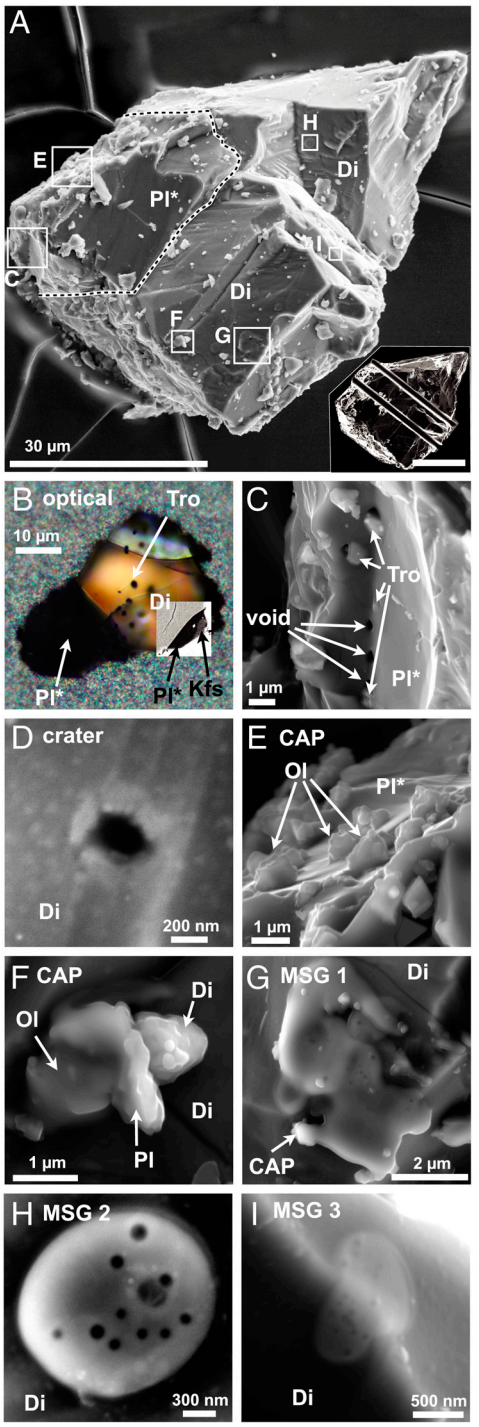

Fig. 3. Surface images of Grain C and its adhered objects, CAPs (common adhered particles) and MSGs (molten splash-shape glasses). (*A*) Entire Grain C. The grain was cut into three pieces by FIB as shown in the insert in the SE of this image. Di and Pl* indicate diopside and diaplectic plagioclase. (*B*) Polarized-reflected-light image obtained for the middle slab with thickness of 15 μm. Troilite (Tro) are included in Di. An occurrence of K-feldspar (Kfs) is shown in the inserted BSE image for the SE part of the slab. (*C*) Microbowls on Pl* substrate partially filled with Tro. Some of these microbowls contain considerable void space. (*D*) Sub-μm-scale crater on a Di substrate. (*E*) CAPs on a Pl* substrate. (*F*) Composite CAP consisting of Ol, plagioclase (Pl), and Di. (*G*) MSG wrapping around CAPs. (*H*) Flattened and convex-disk-shaped MSG with degassing vesicles. (*I*) MSG covering an edge on the surface.

uncertainty of the individual analyses of unknowns is estimated from the spot-to-spot reproducibility (±1 SD, standard deviation), typically 0.5‰ both for $\delta(^{18}O/^{16}O)$ and $\delta(^{17}O/^{16}O)$. The

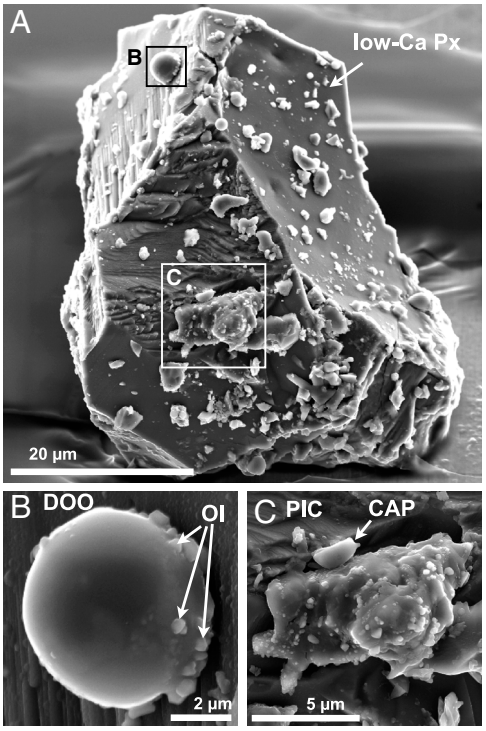

Fig. 4. SEM images of Grain E and adhered objects, DOO (dome-outline objects) and PIC (particularly irregularly-shaped clots). (*A*) The entire Grain E. (*B*) DOO and its spherical morphology. Numerous Fe-rich Ol grains are located at the interface between this DOO and its low-Ca pyroxene (low-Ca Px) substrate. (*C*) PIC consisting of multiple phases, but dominantly sub-μm- to μm-sized merrillite and glass domains and interstitial low-Ca Px and Ol.

in situ analyses demonstrate variation in O isotope compositions within and among phases (Fig. 5*A*, *SI Appendix*, Table S3), with these compositions scattering around those of whole-rock samples of ordinary-chondrites and forming a cluster elongated with a slope of approximately 0.5. The means of ten analyses are 5.2, 4.1, and 1.4‰ for $\delta(^{18}O/^{16}O)$, $\delta(^{17}O/^{16}O)$, and $\Delta(^{17}O/^{16}O)$ $[\equiv\delta(^{17}O/^{16}O) - 0.52\times\delta(^{18}O/^{16}O)]$, respectively. Although one analysis from Grain C overlaps with the terrestrial fractionation (TF) line, within its 1σ analytical uncertainty, the averages estimated from all grains show $\Delta(^{17}O/^{16}O) > 0$. Thus, although the grains have $\delta(^{18}O/^{16}O)$ values very similar to those of mafic and ultramafic rocks on Earth and the moon, they have $\delta(^{17}O/^{16}O)$ different from those of the terrestrial lithologies and thus cannot be derived from a reservoir on Earth. Based on these observations, we confirmed that at least four of the grains are extraterrestrial and derived from the asteroid Itokawa.

Materials from Itokawa's Surface. The most abundant mineral phases observed in the five grains are olivine, low-Ca pyroxene, diopside, and plagioclase. This finding is consistent with that of another recent study of the mineralogy of 1,534 grains from Itokawa (6). The individual constituent minerals, in the different grains, have nearly identical major-element compositions (See *SI Appendix*, Table S1). Standard deviations in the Fe/Mg atomic ratios of olivine and pyroxenes are less than 1%. The Fe/Mg ratios of the phases decrease in the order of olivine (highest), low-Ca pyroxene, and diopside (lowest), and Fe/Mn is higher in olivine than in pyroxenes (Fig. 5*B*). These observations are consistent with the grains having been at an equilibrium condition and, applying two-pyroxene thermometry (16), indicate a temperature of approximately 860°C. Ratios of Fe/Mg and Mn/Fe in olivine and pyroxenes in the Itokawa grains fall within the range for LL-ordinary chondrites (Fig. 5*B*; ref. 17).

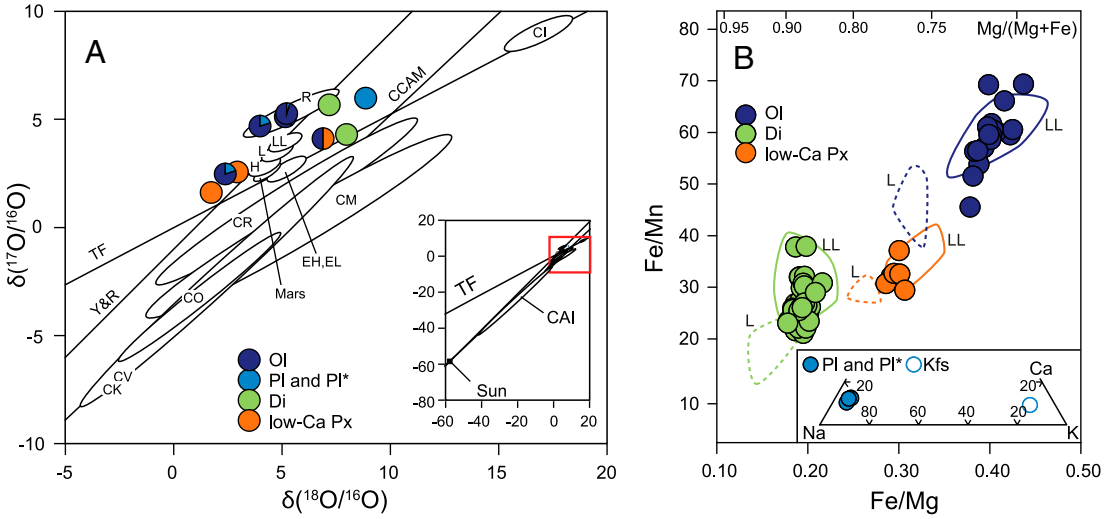

Fig. 5. Oxygen isotope and major element composition. (*A*) Oxygen three-isotope diagram showing silicate minerals collected by the Hayabusa spacecraft and representative compositions of major primary components of solar system matter. This plot includes bulk-rock data for refractory Ca-Al-rich inclusions (CAIs), carbonaceous, ordinary, enstatite, and R chondrites, and Mars. Ion microprobe data for Ol, Pl, Di, and low-Ca Px are indicated by the colored symbols (blue, light blue, green, and orange, respectively). Overlapping data for multiple phases are shown by the pie charts. The relative dimensions of the probed areas are expressed in the charts accordingly. The data for the minerals from Itokawa grains scatter around the range for whole-rock ordinary-chondrites and form an elongated cluster with a slope of approximately 0.5. The means of the analyses for each phase fall into the region for LL-ordinary chondrites defined by Clayton (15). Variation observed in O-isotope compositions is consistent with that observed by Yurimoto, et al. (5) although they interpreted the variation as possibly reflecting analytical ambiguity. (*B*) A diagram to show relative abundance of Mg-Mn-Fe and Na-K-Ca of silicate minerals from Itokawa grains plotted with those in equilibrated (4–6) ordinary chondrites (L and LL).

The occurrences of diaplectic plagioclase and shock lamellae in the olivine are consistent with shock grade S5 (13). Although the overall variation in $\delta(^{18}O/^{16}O)$ in the Itokawa grains is 7‰, larger than the 2‰ expected for equilibrium (18), the major element compositional variations and the record of shock-induced deformation preserved in the grains are similar to those noted for equilibrated LL-ordinary chondrites (14). Thus, together, our observations indicate that the uppermost layer of Itokawa's surface is dominantly composed of equilibrated LL-ordinary-chondrite-like material, a conclusion consistent with that of refs. 5, 6 based on study of other grains from Itokawa.

Grain-Surface Observations. Surfaces of the grains from Itokawa retain textures reflecting the environmental conditions that influenced the physical evolution of the asteroid exterior. The grain surfaces are dominated by fractures, and the fracture planes contain sub-μm-sized craters and adhered objects. These observations suggest the importance, at the asteroidal surface, of the destruction of larger-scale lithic materials by external forces such as repeated impact events. In this section, the craters and adhered objects are described in greater detail.

The occurrences of sub-μm-scale craters (100–200 nm in diameter), on the grain surfaces, provide a record of bombardment by nm-scale projectiles (Fig. 2 *C–E*). Unlike the μm-sized craters with spallation zones developed in lunar samples (19), the rims of the craters on the Itokawa grain consist of chains of seven or eight somewhat irregularly shaped spheres slightly overhanging the pit edges. X-ray mapping (*SI Appendix*, Fig. S7*B*) shows that the olivine substrates and the spheres are identical in major element composition, an observation consistent with spheres having been formed from melts of the olivine grains produced by the high-energy impacts. In the Itokawa grains, the bottoms of the pits were not observed. The diameters of the spheres are approximately half the diameters of the pits, thus the minimum depth of the pits can be calculated as being approximately equal to their diameters. Smaller spheres occur around one crater on a diopside substrate without a well developed rim (Fig. 3*D*), perhaps indicating that the mineralogy of the substrate dictates the morphology of the rim. Assuming that the projectile diameters were an order of magnitude smaller than the diameters of the pits (20) results in estimated projectile sizes of 10–20 nm. The lunar microcraters show a bimodal size distribution, which is attributed from size of projectiles; craters larger than 5 μm are produced by particles spiraling into the Sun whereas the smaller ones are produced by particles propelled away from the Sun by radiation pressure (21). These smaller particles are referred to as β-meteoroids (traveling at >40 km/s) (22). However, radiation pressure for 10-nm-sized particles is orders of magnitude lower than that for typical β-meteoroids, and another physical process to accelerate nm-sized particles is required to explain the formation of the sub-μm-craters.

The adhered objects are another prominent feature of the grain surfaces (Figs. 3 *E–I* and 4 *B* and *C*). We categorize the adhered objects based on morphology as follows: (*i*) common adhered particles (CAPs; Fig. 3 *E* and *F*) making up 90% of the adhered object population and observed at the surfaces of all grains, (*ii*) molten splash-shape glasses (MSGs; Fig. 3 *G–I*) observed on Grains C and D, (*iii*) dome-outline objects (DOOs; Fig. 4*B*) that are relatively large (1–3 μm in diameter) and observed on Grain E, and (*iv*) particularly irregularly-shaped clots (PICs; Fig. 4*C*), aggregates of several lithic materials (two observed on Grain E only). Following are some preliminary interpretations of these widely varying textures.

The CAPs occur as subrounded or flake-like shapes ranging in size from sub-μm to 5 μm (but mostly approximately 1 μm in size). The CAPs are dominantly composed of individual silicate phases (olivine, low-Ca pyroxene, diopside, plagioclase, K-feldspar, and glass) with subordinate troilite, chromite, Cu-sulfide, and Ca-phosphates. Several of the CAPs are associated with multiple phases such as olivine, diopside, and plagioclase (Fig. 3*F*). The silicate mineral modes and chemical compositions of the CAPs are consistent with those of host grains, indicating that most CAPs are fragments of larger grains on Itokawa's surface probably formed by impacts. It is possible that some of the CAPs are of exotic origin because Cu-sulfide is not common in L- or LL-chondrites (23). The CAPs are rigidly fixed on surfaces, but the bonding agent remains uncertain. During the electron-probe

work, the interactions of the electron beam with the CAPs did not displace them from the grain surfaces.

The MSGs (Fig. 3 *G–I*) exhibit irregular shapes (1–5 μm in size) with subcomponents in the shapes of teardrops or rounded disks. MSGs often consist of overlapping layers and appear to wrap around CAPs (Fig. 3*G*). X-ray mapping (*SI Appendix*, Fig. S7*C*) shows that the MSGs and their substrates differ in major element composition. One rounded MSG contains degassing vesicles (Fig. 3*H*), an observation consistent with the origin of the MSGs as melts. The presence of subrounded features covering the edges of some grains (Fig. 3*I*) could suggest that melts approached the surface at significant velocity before solidification. Assuming blackbody thermal radiation, residence times for the melts can be roughly estimated to have been on the order of 10^{-3} s; therefore, it is likely that the melting occurred within m-scale distances from their adhesion sites.

The DOOs are characterized as having rounded morphologies. One DOO on Grain E (Fig. 4*B*) is clearly spheroidal, and this shape and its silica-rich composition ($SiO_2 \sim 70$ wt.%,) suggest that it originated from a relatively viscous melt. Where the DOOs are connected to host objects, rounded sub-μm-sized, Fe-rich olivines are distributed in chain-like fashion. These olivines probably were crystallized from the host melt-spherule during cooling. Unlike for the MSGs, quenching and adhesion appears to have occurred simultaneously for the DOOs. It appears that the transport of silicate melts, likely induced by impacts, was common on the asteroidal surface.

The PIC developed on Grain E (Fig. 4*C*), 10 μm in its longer dimension, consists of multiple phases but is dominantly composed of sub-μm- to μm-sized merrillite and glass. Analyses of interstitial materials demonstrate that they are olivines and low-Ca pyroxenes (*SI Appendix*, Fig. S8). The textures and compositions of the PICs indicate that they represent quenched melt pools. Although the presence of the high-pressure polymorph of merrillite could not be confirmed by micro-Raman spectroscopy (*SI Appendix*, Fig. S9), it is likely that the PICs represent fragments of shock-induced veins, one of the major sites for merrillites observed in ordinary chondrites (24).

In one part of Grain B, three planes were defined based on morphological relationships as F1, F2, and F3, in chronological order assigned by textural observations (Fig. 2*A*). The oldest plane (F1) on olivine exhibits a scaly fabric (Fig. 2*F*). We accidentally produced an additional plane by fracturing during laboratory manipulations. This plane, F4, provides another view of the fabric on F1 (Fig. 2*G*). A sawtooth morphology is observed along F1, and the typical depth and pitch of the sawtooth are 50 and 100 nm, respectively. This sawtooth morphology, not a fracture, suggests on-going modification on F1, and the sharp-edged morphology at the interface suggests that the dominant process was sputtering rather than deposition. The morphology of the scaly fabric implies that surface modification is more effective on physically weaker features such as dislocations related to shock metamorphism. The scaly fabric on F1 suggests that the flux was relatively homogeneous, perhaps pointing to solar wind as the agent for producing this fabric.

Discussion

Asteroid's Surface—Comparison with Spectroscopy. Unprotected by a planetary magnetic field and atmosphere, an asteroid such as Itokawa is continually assailed by micrometeorites and solar wind. In larger-scale studies of asteroid surfaces, based on observations by spectroscopy, the term, space weathering, has become synonymous with darkening or a reduction in band depth in the spectroscopic observations (25). The darkening is thought to reflect the deposition of nano-phase iron on silicate minerals (26) and, accordingly, nano-phase iron particles were found on grains collected from Itokawa (7). Our observations on grain surfaces provide a first demonstration of the sub-micron-scale physical and chemical properties at asteroid exteriors and indicate that space weathering should be regarded as representing a combination of disaggregation, cratering, melting, adhesion, agglutination, and implantation/sputtering. The deposition of nano-phase iron particles represents one result of this complex set of processes. We note that there are several differences in the factors leading to impact features on asteroids and on the Moon, including micrometeorite impact-velocity, surface mineralogy, and particle-size distributions (27).

Although the number of grains examined here was limited to five, many smaller objects were adhered to the grains' surfaces. As described earlier, most of adhered objects were formed during impacts and are likely representative of the asteroid's surface. We examined 914 adhered objects, randomly chosen from the five grains, for their size and chemical composition. The slope of the cumulative size-distribution, for CAPs as solid fragments with sub-μm to several-μm sizes, is −2.31 regardless of the mineralogy of the fragments (Fig. 6; Dataset S1). This slope is similar to the slope of −2.5 expected for a collisional equilibrium distribution with a mass-independent catastrophic disruption threshold (28). MSGs and DOOs with melt morphology clearly show size distributions different from that for fragments of solids. Differences in these distributions reflect the differing physical properties of the ejecta. The evidence for shock-induced melting suggests impact pressures of 50 to 70 GPa, corresponding to projectile velocities of 5 to 10 km/s (29). Based on semiquantitative analyses, each phase of the 914 objects was determined following an algorithm considering contribution of substrate (*SI Appendix*, Fig. S11), and modal abundances of the major silicates were estimated to be 32, 23, 16, 3.9, 1.2, and 25 vol.% for olivine, low-Ca pyroxene, plagioclase, diopside, K-feldspar, and glass, respectively (*SI Appendix*, Table S10). Onboard X-ray fluorescence spectroscopy inferred that the element ratios of Mg/Si and Al/Si of Itokawa's exterior are 0.78 ± 0.09 and 0.07 ± 0.03, respectively (10), and these ratios are very similar to our ratios of 0.72 and 0.08. Near-infrared spectroscopy (NIRS) provided an olivine/(olivine + pyroxene) modal ratio of 0.7 to 0.8 for the average surface material of Itokawa (9), and this is significantly higher than the es-

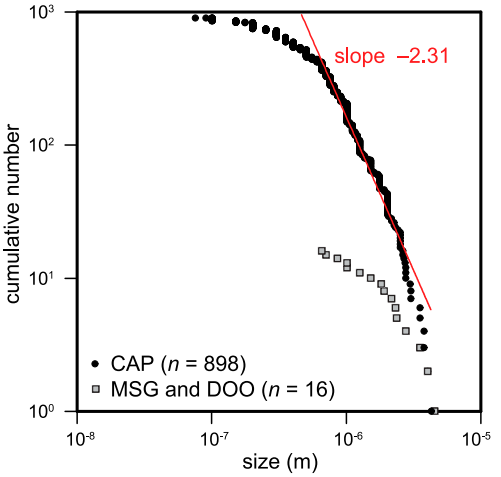

Fig. 6. Cumulative size distribution of solid fragments and quenched melt droplets. Mean of major- and minor-axes of adhered objects randomly chosen was evaluated (Dataset S1). On the log-log plot where grain size is larger than 0.7 μm, quenched melt droplets (MSGs and DOOs, $n = 16$) yield a slope shallower than that estimated from solid fragments (CAPs, $n = 898$). The distribution could be obtained by the splash of melt droplets associated with the shock-induced melting on Itokawa. In the same range, a best-fit slope for solid fragments yields −2.31 (red line). Particles smaller than approximately 1 μm are underrepresented because of their size, therefore, the obtained slope would be somewhat underestimated. The slope suggests catastrophic fragmentation processes by collision cascades might play important role for the evolution of Itokawa's surface.

timate of 0.5 resulting from our analysis. A laboratory simulation using ordinary chondrite suggested that impact melting and subsequent crystallization can modify the spectra (30). In our study, a considerable number of glassy particles were observed on the grain surfaces and the absorption effect of these glassy materials is likely underestimated in the previous model based on NIRS results.

Reconstructed Evolution of an Asteroid. Our observations regarding textures, mineralogy, and geochemistry of the Itokawa grains, together with the results of other recent and ongoing studies, allow a tentative reconstruction of the evolution of Itokawa. A K-feldspar included within plagioclase is regarded as an exsolved phase formed during moderately slow-cooling from the peak metamorphic temperature of 860 °C indicated by the equilibrated major element compositions. However, because of the slower diffusion of O relative to that of the major elements, this metamorphism event did not completely erase the O isotope signatures possibly inherited from the building blocks of the asteroid. This inferred thermal history implies the existence of a larger, pre-Itokawa body. An asteroid radius of several tens of km is required to raise temperatures, by decay of short-lived nuclides, sufficiently to equilibrate silicate major element compositions at temperatures near 900 °C (31). Such temperatures cannot have been attained on the current Itokawa, with its radius of only 300 m. Shock-induced properties such as shock lamellae and diaplectic plagioclase, and the occurrences of PICs, could be indicative of the collisional break-up of a larger asteroid body, the fragments from which were accreted to form the current Itokawa.

It is difficult to ascertain the exact characteristics of the projectiles whose impacts shaped Itokawa's surface; however, the projectiles must have impacted at a significant range of "hypervelocities" to create the nano-size craters and produce adhered objects, including melts, in the inferred sustained fashion. Because of the low escape velocity on Itokawa and on other similar bodies, it is likely that such asteroids are major sources of interplanetary dust particles.

We suggest that the chemistry and textures of Itokawa's surface reflect long-term bombardment of equilibrated chondritic material, at scales of 10^{-9} to 10^{4} meters, and that impact processes in general play a central role in the evolution of planetary bodies. Further surface observations on grains returned by Hayabusa will add statistical significance to the insights regarding solid-to-solid interactions fundamental to our understanding of asteroid accretion and, more broadly, the formation and evolution of interplanetary objects. Needless to say, sampling on other asteroids, and acquisition of age constraints for these bodies, should be the next major conquest.

Materials and Methods

All analyses were undertaken at the Pheasant Memorial Laboratory with nm-scale sample handling capability in part demonstrated by Nakamura, et al. (32). During our study of the Hayabusa grains, we (*i*) determined optical properties, (*ii*) described surface textures and identified constituent phases using a field-emission-type scanning electron microscope (SEM), (*iii*) produced slabbed samples of the grains using a FIB, (*iv*) investigated major element compositions by electron-microprobe techniques, and (*v*) performed in situ analyses, including measurements of O-isotope composition, by SIMS. In this paper, we in particular focused on the grain surface morphology and mineralogy reflecting the physical environment at the asteroidal surface. Greater detail regarding this work is provided in the *SI Appendix*, file linked to the online version of this paper. This file provides Supplemental Methods, Discussion, Tables, Figures, and References related to this initial analysis, including trace-element compositions obtained by SIMS.

ACKNOWLEDGMENTS. The comprehensive analysis we undertook was only possible working as a team. We thank Ikuo Kushiro and the pheasant that in 1992 unknowingly helped launch us on our intellectual quest. We are greatly indebted to T.A. Chekol and S. Tokeshi for their assistance maintaining the laboratory and we thank T. Yamamoto, T. Kadono, S. Ohno, and S. Sasaki for helpful discussions. We are grateful for G. Bebout's efforts editing for clarity and we thank T. Yokoyama, T. Kuritani, and H. Takei for their assistance with the development of analytical methods during the initial stages of our study. Finally, we thank the two anonymous reviewers for their constructive comments.

1. Fujiwara A, et al. (2006) The rubble-pile asteroid Itokawa as observed by Hayabusa. *Science* 312:1330–1334.
2. Saito J, et al. (2006) Detailed images of asteroid 25143 Itokawa from Hayabusa. *Science* 312:1341–1344.
3. Demura H, et al. (2006) Pole and global shape of 25143 Itokawa. *Science* 312:1347–1349.
4. Yano H, et al. (2006) Touchdown of the Hayabusa spacecraft at the Muses Sea on Itokawa. *Science* 312:1350–1353.
5. Yurimoto H, et al. (2011) Oxygen isotopic compositions of asteroidal materials returned from Itokawa by the Hayabusa mission. *Science* 333:1116–1119.
6. Nakamura T, et al. (2011) Itokawa dust particles: a direct link between S-type asteroids and ordinary chondrites. *Science* 333:1113–1116.
7. Noguchi T, et al. (2011) Incipient space weathering observed on the surface of Itokawa dust particles. *Science* 333:1121–1125.
8. Tsuchiyama A, et al. (2011) Three-dimensional structure of Hayabusa samples: origin and evolution of Itokawa regolith. *Science* 333:1125–1128.
9. Abe M, et al. (2006) Near-infrared spectral results of asteroid Itokawa from the Hayabusa spacecraft. *Science* 312:1334–1338.
10. Okada T, et al. (2006) X-ray fuorescence spectrometry of asteroid Itokawa by Hayabusa. *Science* 312:1338–1341.
11. Muller WF, Hornemann U (1969) Shock-induced planar deformation structures in experimentally shock-loaded olivines and in olivines from chondritic meteorites. *Earth Planet Sc Lett* 7:251–264.
12. Weisberg MK (1987) Barred olivine chondrules in ordinary chondrites. *J Geophys Res* 92(B4):663–678.
13. Stöffler D, Keil K, Scott ERD (1991) Shock metamorphism of ordinary chondrites. *Geochim Cosmochim Acta* 55:3845–3867.
14. Kovach HA, Jones RH (2010) Feldspar in type 4-6 ordinary chondrites: metamorphic processing on the H and LL chondrite parent bodies. *Meteorit Planet Sci* 45:246–264.
15. Clayton RN (2003) Oxygen Isotopes in Meteorites. *Meteorites, Comets and Planets: Treatise on Geochemistry,* ed AM Davis pp:129–142.
16. Brey G, Kohler T (1990) Geothermobarometry in four-phase lherzolites II. New thermo-barometers, and practical assessment of existing thermobarometers. *J Petrol* 31:1353–1378.
17. Gastineau-Lyons HK, McSween HY, Jr, Gaffey MJ (2002) A critical evaluation of oxidation versus reduction during metamorphism of L and LL group chondrites, and implications for asteroid spectroscopy. *Meteorit Planet Sci* 37:75–89.
18. Clayton RN, Onuma N, Mayeda TK (1976) A classification of meteorites based on oxygen isotopes. *Earth Planet Sc Lett* 30:10–18.
19. Horz F, et al. (1975) Lunar microcraters: implications for the micrometeoroid complex. *Planet Space Sci* 23:151–152.
20. Holsapple KA (1993) The scaling of impact processes in planetary sciences. *Annu Rev Earth Pl Sc* 21:333–373.
21. Morrison DA, Zinner E (1977) 12054 and 76215—new measurements of interplanetary dust and solar flare fluxes. *Proc Lunar Sc Conf, 8th*, 1 pp:841–863.
22. Carpenter JD, et al. (2007) Nanometer hypervelocity dust impacts in low Earth orbit. *J Geophys Res Planet* 112(E08008), doi:10.1029/2007JE002923.
23. Rubin AE (1997) Mineralogy of meteorite groups. *Meteorit Planet Sci* 32:231–247.
24. Llorca J, Trigo-Rodriguez JM (2006) Raman spectroscopy of merrillite in Villalbeto de la Peña L6 ordinary chondrite. *Lunar Planet Sci XXXVII* abstr:1055.
25. Hapke B (1993) *Theory of Reflectance and Emittance Spectroscopy* (Cambridge University Press, New York) p 455.
26. Sasaki S, Nakamura K, Hamabe Y, Kurahashi E, Hiroi T (2001) Production of iron nanoparticles by laser irradiation in a simulation of lunar-like space weathering. *Nature* 410:555–557.
27. Gaffey MJ (2010) Space weathering and the interpretation of asteroid reflectance spectra. *Icarus* 209:564–574.
28. Tanaka H, Inaba S, Nakazawa K (1996) Steady-state size distribution for the self-similar collision cascade. *Icarus* 123:450–455.
29. Melosh HJ (1989) *Impact Cratering: A Geologic Process* (Oxford University Press, New York) p 253.
30. Moroz LV, Pieters CM, Korotaeva NN (1996) Optical effects of regolith processes on S-asteroids as simulated by laser shots on ordinary chondrite and other magic materials. *Icarus* 122:366–382.
31. Kunihiro T, Rubin AE, McKeegan KD, Wasson JT (2004) Initial $^{26}Al/^{27}Al$ in carbonaceous-chondrite chondrules: Too little ^{26}Al to melt asteroid. *Geochim Cosmochim Acta* 68:2947–2957.
32. Nakamura E, et al. (2003) Comprehensive geochemical analyses of small amounts (<100 mg) of extraterrestrial samples for the analytical competition related to the sample return mission MUSES-C. *ISAS Report SP The First Open Competition for the MUSES-C Asteroidal Sample Preliminary Examination Team* 16:49–101.

Supporting Information

Nakamura et al. 10.1073/pnas.1116236109

SI Methods

Overview. The grains surveyed in this study were collected from the Hayabusa sample-container in a curation facility in Japan Aerospace Exploration Agency (JAXA), Kanagawa, Japan, and transported to Misasa, Tottori. During the trip, each grain was enclosed in a transport case designed specifically for this purpose (see description below). The five grains have JAXA-IDs such as RA-QD02-0121, 0093, 0095, 0118, and 0116, but are hereafter referred to as Grains A–E. Grains A, D, and E arrived in Misasa on May 2, 2011 and the others arrived on April 14, 2011. Procedures undertaken on these grains include sample preparation, surface observation, and chemical examination (*i.e.*, initial analyses), all carried out at the Pheasant Memorial Laboratory (PML; after Nakamura et al., 2003).[32]

After arrival to PML, in which ultraclean conditions are maintained, preliminary observations for each grain were undertaken using optical microscopes. Following the work on optical properties, each grain was transferred from the case to a substrate plate, then prepared (glued) for surface observations using a field-emission-type scanning electron microscopy (FE-SEM). The grains were carbon (C) coated and surface texture was described by a FE-SEM and micro-Raman spectroscopy. Semi-quantitative analyses of the constituent phases and adhered objects were performed on the FE-SEM by energy-dispersive spectroscopy (EDS). Then the grains were sliced into three slabs using a focused-ion beam (FIB) technique. The middle slabs with two flat planes were embedded in an indium (In) pool on an aluminum (Al) disk for further quantitative analyses.

The uppermost layer on each mount was gently polished off then the new surface was acid-leached to minimize contamination during the preparation. After coating with 5 nm of gold (Au), major-element compositions were determined using an electron microprobe analyzer (EMPA). After an additional 60 nm Au coating was added, O isotope composition and trace-element abundances were determined by secondary-ion mass-spectrometry (SIMS).

In this section, the methodology for each step, mentioned above, is described in detail.

Containers for sample transport. We designed a three-fold case assembly to transport the grains from JAXA to PML. An outermost shell consists of a polystyrene box (commercially available as BOXEL, Japan Plus Co. Ltd., Japan) with two polyurethane elasticized membranes inside. By packing the contents with these membranes, the inner contents were tightly held and cushioned in the box and protected from dust, moisture, and shock.

In this box, a pair of petri dishes made of Pyrex (φ 56 mm) functioned as an inner shell (Fig. S1a). A smaller dish was used as a lid for the larger dish. A Viton® O-ring was positioned between the dishes as a seal. An annular-shaped glass plate was located inside this O-ring to hold an innermost container holding the sample. The sample container is a disk made of quartz glass (φ 25 mm, height 5 mm). At the center of the disk, a pit (φ 8 mm) with flat bottom (depth 1 mm) was produced, and a grain was stored in this space (Fig. S1b). A lid made of quartz glass covers the pit, and a plastic spring was located in between the smaller petri dish and the lid to ensure a seal in the container (Fig. S1a).

The sample container, a disk with a pit, was polished using a 0.05-μm alumina paste. Then the glassware, including the sample container, lid, and petri dishes, were washed twice using the following solutions at 80–90 °C for ≥ 12 hours: alkali detergent (5 vol.% TMSC®; Tama Chemical Co. Ltd., Japan), and aqua regia (made of EL grade HCL and HNO_3; Kanto Chemical Co. Ltd., Japan). After the polishing and after each washing, the glassware was cleaned by agitation for 1 hour in an ultrasonic bath (UT-600; Sharp Manufacturing Systems Co. Ltd., Japan) with water of >18 MΩ (Milli-Q®; Millipore Co. Ltd., USA), then dried in a clean bench.

After the cleaning, the surface condition of the pits in the disk was evaluated by SEM. Pieces of quartz glass, likely fragments of the disk, were removed with efficiency of ~80% (initial abundance was 50–100 fragments per pit) by this cleaning. The presence of these remaining pieces (~20% on average) did not hamper identification of the Itokawa grains, which were several tens of μm in size.

To minimize static electricity, the outsides of the disks, the bottoms of the pits, and the lids were coated with 80, 20, and 10 nm of Au, respectively. This Au coating did not significantly alter the transparency of the containers to visible light.

Optical microscopy. The grains in the sample containers, and a slab fabricated from the grains in the In pools, were characterized by optical microscopy, using both transmitted and reflected light. The initial observations characterized each grain as being a silicate phase with opaque inclusions. During a second stage of this optical work, the slabs had thicknesses of ~15 μm and were embedded in the In pool, thus we could obtain polarized- and reflected-light images to evaluate the crystallography of the mineral. We used a Leica Polarizing Microscope DM2500P and a Keyence Digital Microscope VHX-1000 with a VH-Z100UR lens. The grain sizes were determined using the software built into the VXH-1000.

Local sample transfer. After the optical observations were made, each grain was transferred from the container onto a molybdenum (Mo) substrate plate, in a clean bench, using a micro-manipulator system that consists of an oil hydraulic manipulator (Narishige Co. Ltd., Japan) and an optical microscope (model Eclipse FN1; Nikon Co. Ltd., Japan). A needle of clean borosilicate glass, with a tip diameter of 10 μm, was employed for this manipulation to minimize the potential for breaking the grain. Electrostatically, the tip was floated and the container was grounded; this combination passively controlled the electrostatic potential of the tip. A spot of glycol phthalate dissolved in acetone was placed on the plate. The grain was placed on this spot, using the micro-manipulator system, and thus glued onto the substrate. The substrate, with the grain glued onto it, was kept overnight in a box in the clean bench to allow transpiration of the acetone solvent.

Fabrication of grains and preparation of mounts. For a sample-return mission, maintaining the possibility for future repeats of analyses is as important as the initial characterization of the

grains. Thus, we sliced each grain into three pieces; a middle slab was used for our initial study and the other two slabs were stored for future investigation. Focused ion-beam methods (FIB) were applied for the nm-scale site-specific manipulation, using a JEOL JIB-4500 system equipped with a gallium (Ga) ion-gun for sample fabrication, and with the capability of making in-situ observations using a scanning electron beam. Each grain on the Mo substrate was directly loaded into the FIB system. A focused 30 kV Ga^+ ion-beam with a current intensity of 10 nA was employed for slicing of the samples. Sample loss with the slicing was typically a ~3 μm wide zone (Fig. 3a inset, Fig. S2). The thicknesses of the middle pieces (target slabs) were 10–15 μm, of sufficient thickness for the later ion microprobe work.

Using the micro-manipulator system, the fabricated slab was transported from the Mo substrate onto an In pool (φ 5 mm) in an Al disk (φ 25 mm, height 5 mm), along with the reference materials, to minimize analytical uncertainty in *in-situ* O isotope determination related to sample location and topography and electrostatic instability.[33] A separate mount was prepared for each slab sliced from an Itokawa grain. A slab of sample and the reference materials were pressed within the center of the disk, on an In pool, to adjust their surface "elevation" to within 3 μm of the surfaces of the disks (Fig. S3).

To evaluate the sample topography effect, and to ensure accuracy in the O isotope analyses by SIMS, an olivine grain separated from a pallasite, with known O isotope compositions, and a working reference material were embedded within 1 mm lateral distance on an In pool. After an instrumental drift correction using the working reference material, the shift in the $\delta(^{18}O/^{16}O)$ of the pallasite relative to the known value was 0.4‰, comparable to the reproducibility for the working standard. Thus we located sample slabs at the center of the In pools and the reference materials within 1 mm distance of the sample slabs. Reference materials were prepared as follows; (1) thin sections with dimensions of 10 × 10 × 0.1 mm were made for each reference material, (2) these thin sections were polished to reduce surface roughness to less than 0.5 μm, and (3) the thin sections were cut into ~200 μm pieces with a programmable dicing saw, DAD522 (Disco Ltd. Co., Japan). The geochemical properties of the reference materials are listed in Table S5.

In order to remove Ga that precipitated on the slab surfaces during FIB operation, the slabs and diced pieces of the reference materials, embedded together on the In pool with an Al disk, were polished for 10 hours employing a vibratory polisher VibroMet 2 (Buehler, USA) using a polishing cloth MD-Nap (Struers, Denmark) and 0.05-μm alumina-paste. The polished samples were acid-leached with 0.5M HNO_3 and 0.003M HF, for 15 seconds each, to chemically remove surface contamination. Finally, the mounts were coated with 5 nm of Au to prevent charging during the electron microprobe analyses.

Scanning electron microscopic imaging. Before the sample fabrication, surface textures of the grains were observed using a FE-SEM, JEOL JSM-7001F equipped with EDS, Oxford INCA X-Max and X-act energy dispersive X-ray spectrometers. Each grain fixed on a Mo substrate with glycol phthalate was coated with 6 nm of C to prevent charging during the analysis. To observe as many adhered objects on a grain as possible, nearly the entire grain surfaces except for the bottom planes were explored applying a 50° stage tilting combined a 360° stage rotation. The imaging was performed at a 10 kV acceleration voltage and a 1 nA beam current. Quantitative analyses of grain-constituent phases were conducted using a 10 kV acceleration voltage, a 3 nA beam current, and a 75 s integration time. For the adhered objects, the analyses were performed at a 10 kV acceleration voltage and a 0.3 nA beam current. In quantitative analyses, the XPP method[34] was employed for matrix corrections.

The slabs were also investigated using the FE-SEM with a 5 nm thick Au coat, (*e.g.*, Fig. S4). The acceleration voltage and beam current were maintained at 15 kV and 3 nA, respectively. Using this configuration, X-ray maps were obtained for all of the sliced slabs over a 0–10 keV range with 2,000 channels.

Micro-Raman spectroscopy. Confocal micro-Raman spectroscopy was undertaken in order to examine the structural properties of the peculiar phosphate mineral in the PICs adhered onto the surface of Grain E (Fig. 4c). The sample grain on the Mo plate was positioned under a DXR Raman microscope (Thermo Scientific Inc., USA). A 532 nm solid-state laser with a 10 mW power was used as the light source and a spatial resolution of ~0.7 μm was maintained using a 100× objective lens (N.A. = 0.90). Estimated resolution of the Raman shift obtained was 2.7–4.2 cm^{-1} against the 50–3,500 cm^{-1} collection range. Analytical exposure time for each spot was 10 s. Although it was difficult to identify each individual grain under the optical microscope, the significant species of Raman spectra were obtained by applying a 1 μm-step Raman spectroscopy mapping technique.

***In-situ* major elements analysis.** Major-element abundances of phases in the slabs (except for the diaplectic plagioclase) were determined using the EMPA, JEOL JXA-8800R. The quantitative analyses were performed with a 15 kV acceleration voltage and a 12 nA beam current resulting in a 3 μm spot diameter. The oxide ZAF method was employed for matrix corrections and natural and synthetic silicate and oxide minerals were used for calibrations. To avoid the volatilization of Na that occurrs during EMPA analyses, diaplectic plagioclase and associated K-feldspar of Grain C were analyzed by EDS using the FE-SEM. The analytical procedure for use of the FE-SEM with EDS was the same as that described above. Results of these analyses are provided in Fig. 5b and Table S1.

***In-situ* oxygen isotopes analysis.** Oxygen isotope compositions were determined in-situ by SIMS using a Cameca ims-1270. A primary Cs^+ ion beam was accelerated to 10 keV and impacted the sample with an energy of 20 keV. Negatively charged secondary ions were accelerated to –10 keV with an energy band-pass width of 40 eV. A normal incident electron flood gun was used for charge compensation with homogeneous electron density over a circular region with 75 μm diameter.

After the characterization of the polished surface by FE-SEM, the sample surface was coated with an additional 60 nm of Au. A 200 pA Cs^+ primary ion beam was focused to a diameter of 3–4 μm and rastered over a 7 × 7 μm area for 140 s to condition the area of interest. Then the rastered dimensions were reduced to 5 × 5 μm for centering of the secondary beam in an optical gate, followed by mass calibration for 50 s, then data collection for 600 s resulting in an 8 × 8 μm sputtered crater. Secondary ion intensities of $^{16}O^-$, $^{17}O^-$, and $^{18}O^-$ were determined simultaneously in multi-collection mode. The ions of isotopes $^{16}O^-$ and $^{18}O^-$ were collected with a Faraday cup and an electron multiplier (EM), respectively, with mass resolving power ($m/\Delta m$) of 2,400, whereas ions $^{17}O^-$ were collected with the axial EM with $m/\Delta m$ of 7,000 sufficient to eliminate the interfering $^{16}OH^-$ signal. Typical count

rates for $^{16}O^-$, $^{17}O^-$, and $^{18}O^-$ were 3.8×10^7, 1.5×10^4, and 7.5×10^4 counts per second, respectively. The analytical conditions are summarized in Table S2.

The O isotope ratios ($^{18}O/^{16}O$) and ($^{17}O/^{16}O$) are reported in notations of $\delta(^{18}O/^{16}O)$ and $\delta(^{17}O/^{16}O)$, normalized to Vienna standard mean ocean water (VSMOW). We report ^{16}O enrichments relative to the terrestrial fractionation (TF) line as $\Delta(^{17}O/^{16}O) \equiv \delta(^{17}O/^{16}O) - 0.52 \times \delta(^{18}O/^{16}O)$. The relatively high count-rate of the $^{18}O^-$ signal produces a loss in gain due to aging of the first dynode of the EM. The high voltage of the EM was adjusted when necessary to maintain a constant pulse-height distribution. Instrumental mass fractionation (IMF), including mass discrimination and drift of the gain in EMs, was estimated by analyzing a working standard for every two unknown analyses. During a single session, drift of the IMF with time was estimated for both $\delta(^{18}O/^{16}O)$ and $\delta(^{17}O/^{16}O)$. The isotope ratios that were obtained were then corrected to compensate for the analytical artifact contributed from this temporal shift. Differences in mass discrimination owing to the differing mineralogy of the target phase, referred to as the "matrix effect," still remained. To properly estimate the matrix effect requires reference materials with the crystal structure and major-element composition of the target "unknown" phase. We prepared a series of olivines, pyroxenes, and synthetic glasses (the latter with the composition of plagioclase) and the O isotope compositions of these materials were determined by gas-source mass-spectrometry (MAT 253, Thermo Scientific, USA) employing CO_2 laser fluorination extraction methods (data presented in Table S5).

The matrix effect for the target phase was estimated relative to that for the working standard and is believed to result in little shift in $\Delta(^{17}O/^{16}O)$. As noted above, isotope ratios obtained for the target phases were first calibrated using the working standard, then an additional correction for the matrix effect was applied as $\delta(^{18}O/^{16}O) = \delta(^{18}O/^{16}O)^* + \alpha$, where $\delta(^{18}O/^{16}O)^*$ was an isotope ratio calibrated using the working standard and α is the matrix effect for the phase of interest relative to the working standard. The α applied for each phase was determined during each session. San Carlos olivine (fo_{91}), KLB1 clinopyroxene ($wo_{46}en_{49}$), KLB1 orthopyroxene (wo_2en_{88}), and synthesized albite glass (ab_{100}) were embedded along with each slab of an Itokawa grain on its In pool.

For the O isotope measurements, each grain slab was analyzed in a single session, typically with 10 repeated acquisitions for the standard, San Carlos olivine. Typical external precision for the standard during a given session (1 standard deviation; 1SD) was 0.5‰ for both $\delta(^{18}O/^{16}O)$ and $\delta(^{18}O/^{16}O)$, and internal precision ($1\sigma_{mean}$) was 0.2 and 0.4‰ for $\delta(^{18}O/^{16}O)$ and $\delta(^{17}O/^{16}O)$, respectively. Uncertainties in the $\delta(^{18}O/^{16}O)$ measurements are largely due to counting statistics whereas the uncertainties in the $\delta(^{18}O/^{16}O)$ measurements are mainly produced by drift in the EM gain.

After the ion microprobe analyses, the analyzed phases on the sample surface were characterized by FE-SEM using an acceleration voltage of 3 kV and without additional Au coating. For a SIMS analysis that sampled two phases, the relative proportions of the phases in that measurement were thus estimated. Corrections to the matrix effect were applied, assuming that the contributions to the matrix effects by the two phases were proportional to their relative volumetric proportions. Locations of the analyses and the O isotope compositions of those spots are provided in Figs. 5a, S5, and Table S3.

***In-situ* trace elements analysis.** After the *in-situ* O isotope analyses, the abundances of H, Li, B, F, Na, Al, P, Cl, K, Ca, Ti, Cr, Mn, Ni, Sr, Y, Zr, Nb, Ba, La, Ce, Pr, Nd, Sm, Eu, Gd, Dy, Er, Yb, Lu, and Hf were determined by SIMS using a modified Cameca ims-5f. For optimal determinations of these abundances, the elements are divided into four groups such as "HALOGEN (F, P, and Cl)," "LIGHT (H, Li, and B)," "MAJOR-MINOR (Na, Al, K, Ca, Ti, Cr, Mn, and Ni)," and "RARE-EARTH (Sr, Y, Zr, Nb, Ba, La, Ce, Pr, Nd, Sm, Eu, Gd, Dy, Er, Yb, Lu, and Hf)." The analyses for each group were performed sequentially, for the same sample spots, using four different configurations (Table S4).

Primary O^- or Cs^+ ion beams were accelerated to −12.5 or +10 keV to impact the samples with energies of −17 or +14.5 keV, respectively. The elements concerned were positively or negatively accelerated to +4.5 or −4.5 keV. When negative ions were collected, a normal incident electron flood gun was used for charge compensation with homogenous electron density over a circular region with 75 μm diameter. Then the ion intensities for the elements relative to the intensity for Si were determined by magnetic peak-jumping employing an electron multiplier.

To convert from a relative ion intensity obtained on a sample $I(X^+)/I(Si^+)$ to an elemental abundance [X], we first estimated a relative ion yield against Si for the element $Y(X) \equiv \{I(X^+)/I(Si^+)\}/\{n(X)/n(Si)\}$, by analyzing a series of reference materials with known abundance, where X, I, and n correspond to the element being considered, ion intensity, and number of atoms in a unit mass, respectively. Using $Y(X)$, the SiO_2 abundance determined by other techniques, and $I(X^+)/I(Si^+)$, we obtained an elemental abundance [X]. Conversion from ion intensity to elemental abundance on "RARE-EARTH" was slightly more complicated because of significant contributions by oxide interference (e.g., $^nX^+$ has an interference $^{n-16}ZO^+$). To overcome this problem, we analyzed a series of reference materials having different [X]/[Z] and estimated the relative oxide-ion yield $\Psi(Z) \equiv \{I(ZO^+)/I(Si^+)\}/\{n(Z)/n(Si)\}$ as demonstrated in Table S6. Chemical compositions of the reference materials were determined with a thermal-conversion elemental-analyzer and gas-source mass spectrometry (for H), by pyrohydrolysis with ion chromatography (for halogens[35]), by wet chemistry with inductively-coupled-plasma mass-spectrometry (for trace elements including rare-earth elements[36,37,38,39]), or by EMPA (for the rest of the elements that were analyzed). Chemical compositions of all reference materials used to calibrate element abundances are listed in Table S5.

When necessary, before analyses, the mounts were polished with a vibratory polisher, for a few hours, to get a flat surface, then acid-leached as described above, then re-coated with 60 nm of Au. Except in the "RARE-EARTH" configuration, a primary beam with typical diameter of 4 μm was scanned over a 5 × 5 μm area, resulting in a 10 × 10 μm sputtered area less than 1 μm in depth. To minimize contamination from the edge of the sputtered area, an optical gate (field aperture) was inserted, and only secondary ions from the center part, corresponding to a diameter of 8 μm on the sample surfaces, were transferred into the mass spectrometer. Because the craters created in the "RARE-EARTH" analyses had diameters of 10 μm and depths of 6 μm, the "RARE-EARTH" analyses were carried out only after all of the other SIMS analyses.

Detection sensitivity (DS) was calculated from the background signal as follows: $DS \equiv I_{BKG} + 3\sigma_{BKG}$, where I_{BKG} and σ_{BKG} correspond to the mean and one standard deviation of the background signal, respectively. The detection sensitivity is convert-

ed into corresponding element abundance and referred to as the detection limit (*DL*) for each session. During the SIMS sessions, I_{BKG} was significant (1–2 cps), except for the "RARE-EARTH" sessions, for which they were ~0.03 cps. Note that the detection limits for H_2O, P_2O_5, NiO, and B are significantly higher than for the other elements.

Uncertainties were estimated from analyses of reference materials and considered the following: (1) in-run precision (internal precision), (2) among-run reproducibility (external precision), and (3) deviation of self-calibrated abundances, from the reference values (accuracy of calibration curve). These three contributions are comparable in magnitude, and total analytical uncertainties for the trace element analyses would be estimated as 10–20%. However, for some elements, the third ambiguity was notable, significantly increasing the uncertainty. Note that the total analytical uncertainties for H_2O, Na_2O, and MnO are significantly higher than for the other elements.

Analytical results, including the spot locations, relative yields for the target ions, and total analytical uncertainties for the target elements are provided in Tables S6– S7 and Figs. S5–S6.

SI Discussion

Pictorial explanations of each grain. Selected images particularly important for support of the conclusions made in this article are provided in Fig. 3 and Fig. S7. Optical observations provide first-order information regarding grain appearance (morphology), optical property (*e.g.*, pleochroism, anisotropism, birefringence), and internal structure (*e.g.*, mineral inclusions, lamellae, cracks). Electron microscopy provides further detailed information regarding the grain surface, with images of the grains showing multiple stages of fracturing/rupturing, in some cases with overprinting relationships that allow placement into a relative time sequence. Typical morphological features include fractures (linear to conchoidal), micro-cracks, voids, and impact craters. Adhered objects on the grain surfaces are a particularly prominent morphological feature.

Adhered phosphate. A block-like mineral aggregate of one of the PICs (dimensions 10 × 5 μm) is composed of Ca-phosphate, glass, olivine and low-Ca pyroxene (Fig. 4c, Fig. S7e(ix) and Fig. S8). Semi-quantitative analyses of Ca-phosphates by FE-SEM with EDS indicated a chemical formula identical to that of merrillite,[40] $Ca_9MgNa(PO_4)_7$ (Table S9). Micro-Raman spectroscopy was applied in order to clarify the crystallographic structure of this Ca-phosphate. A Raman spectrum obtained for an occurrence in one of the PICs is shown in Fig. S9. This spectrum shows remarkable absorptions at 976 and 961 cm^{-1}, indicating the ν_1 symmetric stretching mode of PO_4^{3-} ions.[41] Other diagnostic absorptions, such as at 1083, 450, 412 cm^{-1}, and some other minor peaks, are identical to those of merrillite with γ-$Ca_3(PO_4)_2$ structure as reported in ordinary chondrites.[24,40,42]

Two different occurrences of merrillite have thus far been reported in ordinary chondrites: (1) as one of the mineral phases associated with glass in shock-induced melt-veins,[24,40,43] and (2) as a phase associated with Fe-Ni metals and Fe sulfide resulting from exsolution and re-crystallization from metal phases during thermal metamorphism.[44,45] In this study, the Raman spectroscopy of merrillite in the PICs did not show a signature of the high-pressure polymorph of Ca-phosphate (γ-$Ca_3(PO_4)_2$ structure);[40,43] however the merrillites are associated with ~1 μm-sized silicate minerals and glass, not with Fe-Ni metal and Fe sulfide, implying melt during rapid cooling. These petrographic features reveal that merrillites in the PICs crystallized from silicate melt pools in the proto-Itokawa body, an origin that has also been suggested for shock-induced veins in ordinary chondrites, but the shock-induced, high-pressure characteristics of the merrillites have not been retained. The lack of these characteristics could be the consequence of annealing of the high-pressure phase at lower pressure conditions during multiple events over Itokawa's long history.

Modal analysis of adhered objects. Individual adhered objects were characterized using FE-SEM equipped with EDS capability. Note that the morphological categories of adhered objects are CAP, MSG, DOO, and PIC, as described in detail in this article. For the 914 adhered objects, properties such as size, composition, and morphological category are summarized in the SI Dataset.

Because the spatial resolution of the EDS analyses is limited to a few μm, the compositions that were determined for these very small objects are regarded as being semi-quantitative. The compositions of the adhered objects are scattered and intermediate between those of olivine, low-Ca pyroxene, diopside and Na-rich plagioclase, as is shown in Fig. S10. One of major analytical artifacts is caused by the contributions from the host grains. Surface roughness and a topography effect also contributed to the uncertainty of these analyses. Neighboring objects contribute a topography effect to the X-ray energy spectra emitted from analyzed areas, that is, there appears to be an energy dependence according to the angle of the solids and the blocking of X-rays by neighboring grains, significantly affecting the resulting spectra.

Identification of the phases in the adhered objects was accomplished based on a combination of analytically obtained compositions and morphology. When an object can be morphologically categorized as being a MSG or DOO, or its abundance of SiO_2 is higher than 70 wt.%, it is identified as glass. In some cases, grains were identified as mineral phases despite deviations from the expected chemical stoichiometry for that phase, possibly resulting in an underestimation of the amounts of glass. Fig. S11 shows a flow chart of the steps taken in determining the phases present in an adhered object. First, spinel and sulfide were identified, as were any glass present (based on textures and/or SiO_2 content) and Ca-phosphates and K-feldspar (based on the abundances of P_2O_5 and K_2O). Then, the remaining objects were classified as being olivine, plagioclase, diopside, or low-Ca pyroxene. Note that plagioclase with Al_2O_3 abundance lower than 3 wt.% is classified as being glass.

After the phase identifications, we calculated the volumes of each object, assuming spheroidal shapes with the measured major and minor axis dimensions. We then summed these up for each phase, allowing estimates of modal abundances (Table S10).

Trace-element abundances. We noticed that some elements of concern have interferences related to the abundance of In in the sample mounts (Table S8). Contributions from In-related molecule ions were significant in measurements of the concentrations of Ba and the light rare-earth element (REE) such as $^{137}Ba^+$, $^{139}La^+$, $^{140}Ce^+$, $^{141}Pr^+$, and $^{147}Sm^+$. This led to difficulties in the determinations of concentrations of $^{151}Eu^+$, $^{157}Gd^+$, $^{163}Dy^+$, $^{167}Er^+$, $^{174}Yb^+$, $^{175}Lu^+$, and $^{178}Hf^+$ because of interferences from oxide ions of these Ba and slight REEs. The olivines and low-Ca pyroxenes on the In matrix mount showed zig-zagged light-REE-elevated patterns; however, diopside and diaplectic plagioclase did not (spots 8 and 9 on the slab of Grain C; see Fig. S5). The inter-

ferences are considered to be from In-Mg molecules (except for $^{147}Sm^{+}$, that shows interference from an In oxide; see Table S8). The ion intensity of the interfering ions is not only a function of distance from the In matrix, but also the Mg abundance in the target silicate phase. Patterns that have obviously experienced interference, observed for olivines and low-Ca pyroxenes, probably resulted from a combination of their higher Mg contents and their low trace-element abundances, compared to diopside and diaplectic plagioclase. Available data of trace element abundances determined in this study are shown in Table S7. As mentioned, full sets of "RARE-EARTH" abundances would be available only for diopside and diapleptic plagioclase of Grain C.

In Grain C (Fig. S6), both the diopside and the diaplectic plagioclase yielded REE abundances slightly higher than those of the L/LL4–6 chondrites. The diopside exhibits a slightly light-REE-depleted pattern with a negative Eu anomaly, and the diapleptic plagioclase shows a flat pattern with a positive Eu anomaly. This relationship is suggestive of a co-genetic relationship between these two phases. The Li-depleted patterns for diopside and diapleptic plagioclase in Grain C are perhaps indicative of later aqueous alteration processes.

33. Kita NT, Ushikubo T, Fu B, Valley JW (2009) High precision SIMS oxygen isotope analysis and the effect of sample topography. *Chem Geol* 264: 43–57.
34. Pouchou J, Pichoir F (1998) A simplified version of the pap model for matrix corrections in EPMA. In D. Newbury (Ed.), *MICROBEAM ANALYSIS*. (San Francisco Press, San Francisco, California): 315–318.
35. Wang Q, Makishima A, Nakamura E (2010) Determination of fluorine and chlorine by pyrohydrolysis and ion chromatography: Comparison with alkaline fusion digestion and ion chromatography. *Geostand Geoanal* Res 34: 175–183.
36. Makishima A, Nakamura E (1997) Suppression of matrix effect in ICP-MS by high power operation of ICP: Application to precise determination of Rb, Sr, Y, Cs, Ba, REE, Pb, Th and U at ng/g levels in a few milligram silicate sample. *Geostand Newslett* 21: 307–319.
37. Makishima A, Nakamura E, Nakano T (1999) Determination of zirconium, niobium, hafnium and tantalum at ng g^{-1} levels in geological materials by direct nebulization of sample HF solution into FI-ICP-MS. *Geostand Newslett* 23: 7–20.
38. Yokoyama T, Makishima A, Nakamura E. (1999) Evaluation of the coprecipitation of incompatible trace elements with fluoride during silicate rock dissolution by acid digestion. *Chem Geol* 157: 175–187.
39. Moriguti T, Makishima A, Nakamura E (2004) Determination of lithium contents in silicates by isotope dilution ICP-MS and its evaluation by isotope dilution thermal ionisation mass spectrometry. *Geostand Geoanal Res* 28: 371–382.
40. Xie X, et al. (2002) Natural high-pressure polymorph of merrillite in the shock veins of the Suizhou meteorite. *Geochim Cosmochim Acta* 66: 2439–2444.
41. Mooney RW, Toma SZ, Goldsmith RL, Butler KH (1968) Normal vibrations of the PO_4^{3-} ion, site symmetry C_{3v} in $Sr_3(PO_4)_2$ and $Ba_3(PO_4)_2$. *J Inorg Nucl Chem* 30: 1669–1675.
42. Cooney TE, Scott ERD, Krot AN, Sharma SK, Yamaguchi A (1999) Vibration spectroscopic study of minerals in the Martian meteorite ALH84001. *Am Min* 84: 1569–1576.
43. Chen M, Wopenka B, Xie X, El Goresy AA (1995) New high-pressure polymorph of chlorapatite in the shocked Siziangkou (L6) chondrite. *Lunar Planet Sci XXVI*: 237–238.
44. Zanda B, Bourot-Denise M, Perron C, Hewins R (1999) Origin and metamorphic redistribution of silicon, chromium, and phosphorus in the metal of chondrite. *Science* 265: 1846–1849.
45. Dreeland L, Jones RH (2011) Origin and development of phosphate minerals in metamorphosed LL chondrites. *Lunar Planet Sci XLII abstr*: 2523.
46. Friedrich JM, Bridges JC, Wang M-S, Lipschutz ME (2004) Chemical studies of L chondrites. VI: variations with petrographic type and shock-loading among equilibrated falls. *Geochim Cosmochim Acta* 68: 2889–2904.
47. Friedrich JM, Wang M-S, Lipschutz ME (2003) Chemical studies of L chondrites. V: compositional patterns for 49 trace elements in 14 L4–6 and 7 LL4–6 falls. *Geochim Cosmochim Acta* 67: 2467–2479.
48. Anders E, Grevesse N (1989) Abundances of the elements: Meteoritic and solar. *Geochim Cosmochim Acta* 53: 197–214.

Table S1. Major-element compositions of the Itokawa grains. Concentrations (in wt.%) were determined by EMPA for all phases except for feldspars in Grain C. Concentrations less than 0.1 wt.% were treated as being "below detection limit" and indicated by a dash. Variations among spots are shown as 1σ in parentheses. Mg# is defined as 100 × Mg/(Mg+Fe) in atomic abundances. Analyses of feldspars in Grain C were carried using an FE-SEM with EDS capability, where concentrations less than 0.2 wt.% were treated as being "below detection limit" and the total abundance of oxides was normalized to 100 wt.%. Abbreviations: Ol—olivine; low-Ca Px—low-Ca pyroxene; Di—diopside; Pl—plagioclase; Pl*—diaplectic plagioclase; Kfs—K-feldspar.

Target	Grain A				Grain B				Grain C						Grain D	
Phase	$Ol_{n=2}$		low-Ca $Px_{n=2}$		$Ol_{n=12}$		$Pl_{n=6}$		$Di_{n=51}$		$Pl^*_{n=8}$		$Kfs_{n=2}$		low-Ca $Px_{n=5}$	
SiO_2	39.61	(1.59)	53.85	(1.06)	38.93	(0.95)	65.40	(0.74)	54.08	(0.40)	66.95	(0.77)	62.06	(0.28)	56.76	(0.11)
TiO_2	-		0.18	(0.01)	-		-		0.40	(0.04)	-		-		0.19	(0.05)
Al_2O_3	-		0.41	(0.32)	-		20.43	(0.56)	0.49	(0.04)	20.91	(0.16)	19.34	(0.26)	0.17	(0.09)
Cr_2O_3	-		-		-		0.17	(0.03)	0.75	(0.05)	-		-		0.12	(0.01)
FeO	24.57	(1.13)	15.38	(0.19)	26.26	(0.44)	0.65	(0.19)	5.59	(0.18)	0.25	(-)	0.22	(-)	15.14	(0.43)
NiO	-		-		-		-		-		0.35	(0.13)	-		-	
MnO	0.49	(0.03)	0.49	(0.02)	0.44	(0.03)	-		0.21	(0.03)	-		-		0.46	(0.03)
MgO	35.97	(1.03)	28.42	(0.73)	36.94	(0.81)	0.40	(0.26)	16.15	(0.22)	-		-		28.86	(0.41)
CaO	-		0.61	(0.12)	-		2.36	(0.16)	20.94	(0.37)	2.28	(0.10)	2.16	(0.02)	0.66	(0.03)
Na_2O	-		-		-		8.93	(0.31)	0.54	(0.05)	8.78	(1.09)	1.06	(0.11)	-	
K_2O	-		-		-		0.97	(0.08)	-		0.94	(0.16)	15.27	(0.07)	-	
total	101.4		99.3		102.9		99.1		99.1		100		100		102.4	
Formula	fo_{72}		wo_1en_{75}		fo_{71}		$an_{12}ab_{82}or_6$		$wo_{44}en_{45}$		$an_{12}ab_{82}or_6$		$an_{10}ab_8or_{82}$		wo_1en_{76}	
Mg#	72	(0.4)	76	(0.2)	71	(0.6)			84	(0.5)					77	(0.4)
$(Fe/Mg)_{atom}$	0.38		0.3		0.4				0.2						0.29	
$(Fe/Mn)_{atom}$	49		31		59				26						32	

Table S2. Analytical conditions for the *in-situ* oxygen isotope analyses.

Instrument	Cameca ims-1270
Primary beam ion	+20 keV Cs^+
Gold coat thickness	65 nm
Secondary accelerating voltage	−10 kV
Primary beam current	200 pA
Primary beam rastering	5 × 5 μm (7 × 7 μm for first 140 s)
Energy offset	−45 eV
Contrast aperture diameter	40 μm
Entrance slit width	80 μm
Field aperture dimension	800 × 800 μm (20 × 20 μm on sample)
Energy band pass	from −10 to +30 eV
Exit slit width	200 μm for $^{17}O^-$, and 400 μm for $^{16}O^-$ and $^{18}O^-$
Mass resolution power ($m/\Delta m$)	7,000 for $^{17}O^-$, and 2,400 for $^{16}O^-$ and $^{18}O^-$
Detectors	FC (L'2) for $^{16}O^-$, EM (axial) for $^{17}O^-$, and EM (H1) for $^{18}O^-$
Beam optimization	automatic FA centering at beginning (30 s)
Mass calibration	automatic mass centering at beginning (15 s)
Pre-sputter duration	3 min 10 s including beam optimization and mass calibration
Secondary ion integration	14.5 s × 40 cycles

Table S3. Results of *in-situ* O isotope analyses. For analyses sampling two phases, proportions of the two phases are indicated. Analytical uncertainty is estimated to be ~0.5‰ ($1\sigma_{mean}$) for $\delta(^{18}O/^{16}O)$, $\delta(^{17}O/^{16}O)$, and $\Delta(^{17}O/^{16}O)$.

Target	Spot	Phase	$\delta(^{18}O/^{16}O)$	$\delta(^{17}O/^{16}O)$	$\Delta(^{17}O/^{16}O)$
Grain A	802	$Ol_{0.5}$ low-Ca $Px_{0.5}$	6.9	4.1	0.5
Grain B	694	$Ol_{0.95}$ $Pl_{0.05}$	5.2	5.2	2.5
	720	$Ol_{0.8}$ $Pl_{0.2}$	2.4	2.5	1.3
	721	$Ol_{0.8}$ $Pl_{0.2}$	4.0	4.6	2.5
	723	$Ol_{0.6}$ $Pl_{0.4}$	5.1	5.0	2.3
Grain C	755	Di	7.2	5.5	1.8
	756	Di	8.0	4.2	0.1
	765	Pl*	8.8	5.8	1.2
Grain D	782	low-Ca Px	2.9	2.6	1.1
	783	low-Ca Px	1.7	1.7	0.8

Table S4. Analytical conditions for the *in-situ* trace element analyses.

Session	"HALOGEN"	"LIGHT"	"MAJOR-MINOR"	"RARE-EARTH"
Analyzed ion	$^{19}F^-$, $^{28}Si^-$, $^{31}P^-$, $^{35}Cl^-$	$^{1}H^+$, $^{7}Li^+$, $^{11}B^+$, $^{28}Si^+$	$^{23}Na^+$, $^{27}Al^+$, $^{28}Si^+$, $^{39}K^+$, $^{42}Ca^+$, $^{46}Ti^+$, $^{52}Cr^+$, $^{55}Mn^+$, $^{60}Ni^+$	$^{7}Li^+$, $^{30}Si^+$, $^{88}Sr^+$, $^{89}Y^+$, $^{90}Zr^+$, $^{93}Nb^+$, $^{137}Ba^+$, $^{139}La^+$, $^{140}Ce^+$, $^{141}Pr^+$, $^{146}Nd^+$, $^{147}Sm^+$, $^{151}Eu^+$, $^{157}Gd^+$, $^{163}Dy^+$, $^{167}Er^+$, $^{174}Yb^+$, $^{175}Lu^+$, $^{178}Hf^+$
Primary beam ion	+14.5 keV Cs^+	−17 keV O^-	−17 keV O^-	−17 keV O^-
Primary beam current	200 pA	−500 pA	−500 pA	−5 nA
Primary beam rastering	5 × 5 μm	5 × 5 μm	5 × 5 μm	—
Energy offset	—	—	—	−45 eV
Contrast aperture size	150 μm	150 μm	150 μm	400 μm
Entrance slit width	10 μm	20 μm	10 μm	400 μm
Field aperture diameter	100 μm	100 μm	100 μm	1,800 μm
Energy band pass	from −50 to +50 eV	from −50 to +50 eV	from −50 to +50 eV	from −20 to +20 eV
Exit slit width	50 μm	100 μm	50 μm	800 μm
Mass resolution power ($m/\Delta m$)	2,400	1,500	2,400	500
Pre-sputter duration	540 s	720 s	600 s	120 s

Table S5. Geochemical properties of the reference glasses and minerals preared for the *in-situ* analyses. Dashes indicate that data are not available.

Phase	glass						
ID	gl-tahiti	gl-hawaii	gl-dr1a1	gl-pjr1	gl-myk1-1	gl-myk1-2	gl-myk1-5
SiO_2 (wt.%)	59.00	51.20	51.30	76.10	53.50	53.90	54.60
TiO_2	0.73	2.45	1.24	0.35	1.35	1.30	1.39
Al_2O_3	18.31	13.64	16.65	11.87	15.59	15.60	15.66
Cr_2O_3	-	-	-	-	-	-	-
FeO	4.80	11.13	7.95	1.44	11.92	11.07	10.72
NiO	-	-	-	-	-	-	-
MnO	-	-	-	-	0.47	0.46	-
MgO	0.81	6.49	5.83	-	3.12	3.13	2.97
CaO	1.81	10.66	10.97	0.52	8.94	9.05	8.90
Na_2O	6.83	2.59	3.33	3.75	3.28	3.11	3.24
K_2O	6.69	0.46	0.34	5.69	0.55	0.68	0.56
P_2O_5	-	-	-	-	-	-	-
H_2O	-	-	0.26	0.12	-	-	-
Li ($\mu g \cdot g^{-1}$)	20.8	4.4	8.7	-	-	-	-
B	12.4	1.6	-	-	-	-	-
F	-	-	-	-	29	114	566
Cl	-	-	-	-	184	295	868
Sr	107	349	178	-	-	-	-
Y	63	30	36	-	-	-	-
Zr	1305	142	90	-	-	-	-
Nb	150	11	3.7	-	-	-	-
Ba	277	102	21	-	-	-	-
La	117	11	4.4	-	-	-	-
Ce	254	29	12	-	-	-	-
Pr	29	4.1	1.9	-	-	-	-
Nd	111	21	10	-	-	-	-
Sm	20	5.4	3.3	-	-	-	-
Eu	4.7	1.9	1.2	-	-	-	-
Gd	16	5.8	3.9	-	-	-	-
Dy	12	5.5	5.1	-	-	-	-
Er	5.3	2.6	3	-	-	-	-
Yb	4.8	2.3	3.2	-	-	-	-
Lu	0.71	0.31	0.46	-	-	-	-
Hf	29	3.8	2.5	-	-	-	-
Δ ($^{18}O/^{16}O$)	-	-	-	-	-	-	-
Δ ($^{17}O/^{16}O$)	-	-	-	-	-	-	-

Table S5 (continued). Geochemical properties of the reference glasses and minerals prepared for the *in-situ* analyses.

Phase	glass		apatite	pyroxene			
ID	gl-nist610	gl-ab1	ap-durango	cpx-klb1	cpx-sag30	cpx-sax39	opx-klb1
SiO_2 (wt.%)	70.50	69.13	0.41	51.95	53.40	53.40	54.81
TiO_2	-	-	-	0.54	1.07	0.72	0.14
Al_2O_3	1.50	19.63	-	7.28	5.23	5.69	5.15
Cr_2O_3	-	-	-	0.78	1.08	0.10	0.39
FeO	-	-	-	3.08	3.38	6.50	6.45
NiO	-	-	-	-	-	-	0.20
MnO	-	-	-	0.11	0.10	0.13	0.17
MgO	-	-	-	14.87	17.10	16.97	32.15
CaO	10.76	-	53.07	19.38	16.75	13.91	0.85
Na_2O	14.63	14.55	-	1.76	1.91	2.13	0.13
K_2O	-	-	-	-	-	-	-
P_2O_5	-	-	44.05	-	-	-	-
H_2O	-	-	-	-	-	-	-
Li ($\mu g \cdot g^{-1}$)	485	-	-	1.4	1.7	3.1	-
B	356	-	-	-	-	0.5	-
F	-	-	34700	-	-	-	-
Cl	-	-	4100	-	-	-	-
Sr	-	-	-	36	117	74	-
Y	-	-	-	24	7.0	6.0	-
Zr	-	-	-	29	41	19	-
Nb	-	-	-	0.01	0.35	0.15	-
Ba	-	-	-	0.18	0.36	0.24	-
La	-	-	-	0.23	1.7	0.87	-
Ce	-	-	-	1.8	6.5	3.5	-
Pr	-	-	-	0.49	1.3	0.69	-
Nd	-	-	-	-	8.0	4.6	-
Sm	-	-	-	1.7	2.6	1.7	-
Eu	-	-	-	0.71	0.82	0.55	-
Gd	-	-	-	2.6	2.5	1.7	-
Dy	-	-	-	3.7	1.7	1.5	-
Er	-	-	-	2.2	0.48	0.53	-
Yb	-	-	-	2.1	0.26	0.32	-
Lu	-	-	-	0.3	0.03	0.04	-
Hf	-	-	-	0.99	2.0	1.1	-
Δ ($^{18}O/^{16}O$)	-	18.45	-	5.45	-	-	5.76
Δ ($^{17}O/^{16}O$)	-	9.39	-	2.85	-	-	3.04

Table S5 (continued). Geochemical properties of the reference glasses and minerals prepared for the in-situ analyses.

Phase			olivine			garnet	
ID	ol-fa-hk1	ol-sc5	ol-sc1	ol-fo1	ol-fukang1	grt-hk5206701d	grt-mnag10
SiO_2 (wt.%)	30.80	41.50	42.06	43.34	41.34	40.50	42.40
TiO_2	-	-	-	-	-	0.14	1.16
Al_2O_3	-	-	-	-	-	22.52	21.22
Cr_2O_3	-	-	-	-	-	-	0.61
FeO	65.08	8.72	8.57	1.05	13.42	20.75	10.38
NiO	-	0.42	0.37	-	-	-	-
MnO	5.09	0.12	0.15	-	0.34	0.50	0.30
MgO	0.51	51.19	51.59	57.68	48.44	11.64	19.76
CaO	-	0.10	-	-	-	4.45	4.47
Na_2O	-	-	-	-	-	-	0.12
K_2O	-	-	-	-	-	-	-
P_2O_5	-	-	-	-	-	-	-
H_2O	-	-	-	-	-	-	-
Li ($\mu g \cdot g^{-1}$)	-	-	-	-	-	-	0.4
B	-	-	-	-	-	-	0.1
F	-	-	-	-	-	-	-
Cl	-	-	-	-	-	-	-
Sr	-	-	-	-	-	-	1.0
Y	-	-	-	-	-	-	46
Zr	-	-	-	-	-	-	107
Nb	-	-	-	-	-	-	0.21
Ba	-	-	-	-	-	-	0.07
La	-	-	-	-	-	-	0.06
Ce	-	-	-	-	-	-	0.47
Pr	-	-	-	-	-	-	0.17
Nd	-	-	-	-	-	-	1.8
Sm	-	-	-	-	-	-	1.6
Eu	-	-	-	-	-	-	0.84
Gd	-	-	-	-	-	-	3.6
Dy	-	-	-	-	-	-	6.8
Er	-	-	-	-	-	-	4.7
Yb	-	-	-	-	-	-	5.1
Lu	-	-	-	-	-	-	0.72
Hf	-	-	-	-	-	-	2.8
Δ ($^{18}O/^{16}O$)	-	-	5.27	23.6	3.46	-	-
Δ ($^{17}O/^{16}O$)	-	-	2.78	12.4	1.64	-	-

Table S6. Ion yield, typical sensitivity, detection limit and total analytical uncertainty of analyzed elements and related oxides. † and ‡ indicate results obtained in "LIGHT" and "RARE-EARTH" sessions, respectively. DL indicates the detection limit; numbers in brackets are oxide equivalents. See SI Methods for estimating detection limit and total analytical uncertainty. Note that ion yields for F, Cl, and P are for negative ions.

	Yield (relative to Si)	Sensitivity (cps/nA/μg·g^{-1})	DL (μg·g^{-1})		Uncertainty (%)	Reference material
H	0.05	0.1	20	[200]	50	gl-dr1a1, gl-pjr1
Li†	6.8	14	1		20	gl-tahiti, gl-hawaii, gl-dr1a1, gl-nist610
Li‡	1.3	14	0.01		10	gl-tahiti, gl-hawaii, gl-dr1a1, cpx-klb1
B	0.5	0.5	30		10	gl-tahiti, gl-nist610
F	27	18	2		10	gl-myk1-1, gl-myk1-2, gl-myk1-5, ap-durango
Na	19	2.7	4	[6]	40	gl-dr1a1, cpx-klb1 grt-mnag10, gl-nist610
Al	4.8	0.4	20	[40]	20	grt-mnag10, gl-hawaii, cpx-klb1, gl-nist610
P	0.9	0.2	80	[200]	10	ap-durango
Cl	22	9.0	4		20	gl-myk1-1, gl-myk1-2, gl-myk1-5, ap-durango
K	21	2.7	5	[6]	30	gl-pjr1, gl-hawaii, gl-dr1a1, gl-nist610
Ca	11	1.0	10	[20]	20	cpx-klb1, grt-hk5206701d, gl-pjr1, ol-sc5
Ti	4.1	0.2	50	[80]	10	gl-hawaii, cpx-sag30, gl-tahiti, grt-hk5206701d
Cr	4.4	0.2	60	[80]	10	cpx-sag30, grt-mnag10
Mn	3.9	0.2	60	[80]	30	ol-fa-hk1, grt-hk5206701d, grt-mnag10, cpx-sag30
Ni	1.0	0.04	300	[400]	10	ol-sc5
Sr	3.0	2.1	0.04		10	gl-tahiti, gl-hawaii, gl-dr1a1, cpx-klb1
Y	2.3	2.1	0.04		10	gl-tahiti, gl-hawaii, gl-dr1a1, cpx-klb1
Zr	2.2	1.1	0.1		10	gl-tahiti, gl-hawaii, gl-dr1a1, cpx-klb1
Nb	1.4	1.4	0.1		10	gl-tahiti, gl-hawaii, gl-dr1a1, cpx-klb1
Ba	2.1	0.2	0.4		20	gl-tahiti, gl-hawaii, gl-dr1a1, cpx-klb1
La	1.9	1.2	0.1		10	gl-tahiti, gl-hawaii, gl-dr1a1, cpx-klb1
Ce	1.8	0.9	0.1		10	gl-tahiti, gl-hawaii, gl-dr1a1, cpx-klb1
Pr	2.1	1.2	0.1		10	gl-tahiti, gl-hawaii, gl-dr1a1, cpx-klb1
Nd	2.1	0.2	0.4		10	gl-tahiti, gl-hawaii, gl-dr1a1, cpx-klb1
Sm	2.4	0.2	0.4		10	gl-tahiti, gl-hawaii, gl-dr1a1, cpx-klb1
Eu	2.4	0.8	0.1		20	gl-tahiti, gl-hawaii, gl-dr1a1, cpx-klb1
BaO	0.2	—	—		—	gl-tahiti, gl-hawaii, gl-dr1a1, cpx-klb1
Gd	2.3	0.5	0.1		10	gl-tahiti, gl-hawaii, gl-dr1a1, cpx-klb1
PrO	0.8	—	—		—	gl-tahiti, gl-hawaii, gl-dr1a1, cpx-klb1
Dy	1.8	0.3	0.2		10	gl-tahiti, gl-hawaii, gl-dr1a1, cpx-klb1
SmO	0.9	—	—		—	gl-tahiti, gl-hawaii, gl-dr1a1, cpx-klb1
Er	1.5	0.3	0.2		20	gl-tahiti, gl-hawaii, gl-dr1a1, cpx-klb1
EuO	0.8	—	—		—	gl-tahiti, gl-hawaii, gl-dr1a1, cpx-klb1
Yb	1.7	0.5	0.1		20	gl-tahiti, gl-hawaii, gl-dr1a1, cpx-klb1
GdO	0.7	—	—		—	gl-tahiti, gl-hawaii, gl-dr1a1, cpx-klb1
Lu	1.0	1.4	0.1		30	gl-tahiti, gl-hawaii, gl-dr1a1, cpx-klb1
TbO	0.7	—	—		—	gl-tahiti, gl-hawaii, gl-dr1a1, cpx-klb1
Hf	1.0	0.2	0.4		10	gl-tahiti, gl-hawaii, gl-dr1a1, cpx-klb1
DyO	0.3	—	—		—	gl-tahiti, gl-hawaii, gl-dr1a1, cpx-klb1

Table S7. Chemical compositions of the Itokawa grains determined using the Cameca ims-5f ion microprobe. Abundances are expressed in a unit of μg·g^{-1} except for SiO_2. In-run uncertainty ($1\sigma_{mean}$) is provided in parentheses. Note that SiO_2 concentration (wt.%) is obtained by electron microprobe analyses (Table S1). For analyses sampling two phases, proportions of the two phases are indicated, and SiO_2 concentration§ was assumed accounting these proportions. Dashes and dots indicate "not available" and "not analyzed," respectively. † and ‡ were obtained in "LIGHT" and "RARE-EARTH" sessions, respectively.

Target	Grain A		Grain B		Grain B		Grain B		Grain B		Grain B	
Spot	1		2		3		4		5		6	
Phase	$Ol_{0.5}$ low-Ca $Px_{0.5}$		Ol		$Ol_{0.9}Pl_{0.1}$		Pl		$Pl_{0.3}Ol_{0.7}$		$Pl_{0.6}Ol_{0.4}$	
SiO_2	*46.73*	§	*38.93*		*41.58*	§	*65.40*		*46.87*	§	*54.81*	§
TiO_2	1,500	(52)	-	(19)	• • •		360	(70)	• • •		• • •	
Al_2O_3	1,800	(25)	430	(10)	• • •		15,000	(840)	• • •		• • •	
Cr_2O_3	780	(11)	-		• • •		1,700	(390)	• • •		• • •	
FeO	• • •		• • •		• • •		• • •		• • •		• • •	
NiO	-		-		• • •		-		• • •		• • •	
MnO	5,400	(31)	7,100	(50)	• • •		1,200	(23)	• • •		• • •	
MgO	• • •		• • •		• • •		• • •		• • •		• • •	
CaO	5,300	(201)	110	(50)	• • •		15,000	(540)	• • •		• • •	
Na_2O	46	(1)	120	(2)	• • •		40,000	(380)	• • •		• • •	
K_2O	-		19	(1)	• • •		6,100	(83)	• • •		• • •	
P_2O_5	-		720	(10)	• • •		2,100	(210)	• • •		• • •	
H_2O	680	(8)	690	(15)	• • •		350	(9)	• • •		• • •	
Li†	-		7.9	(0.1)	• • •		3.0	(0.1)	• • •		• • •	
Li‡	0.60	(0.04)	2.7	(0.1)	2.7	(0.2)	• • •		0.9	(0.1)	2.5	(0.4)
B	-		-		• • •		-		• • •		• • •	
F	29	(2)	4.3	(0.3)	• • •		36	(1)	• • •		• • •	
Cl	6.6	(0.4)	-		• • •		11	(1)	• • •		• • •	
Sr	0.13	(0.01)	5.2	(0.4)	18	(4)	• • •		46	(5)	70	(13)
Y	0.32	(0.02)	0.26	(0.13)	0.17	(0.07)	• • •		0.8	(0.1)	45	(8)
Zr	0.92	(0.06)	0.44	(0.09)	1.4	(0.1)	• • •		2.0	(0.4)	2.7	(0.4)
Nb	2.7	(0.2)	0.74	(0.27)	2.0	(1.5)	• • •		11	(1)	38	(7)
Ba	-		-		-		• • •		-		-	
La	-		-		-		• • •		-		-	
Ce	-		-		-		• • •		-		-	
Pr	-		-		-		• • •		-		-	
Nd	-		-		-		• • •		0.37	(0.001)	6.9	(1.2)
Sm	-		-		-		• • •		-		-	
Eu	-		-		-		• • •		-		-	
Gd	-		-		-		• • •		-		-	
Dy	-		-		-		• • •		-		-	
Er	-		-		-		• • •		-		-	
Yb	-		-		-		• • •		-		-	
Lu	-		-		-		• • •		-		-	
Hf	-		-		-		• • •		-		-	

Table S7 (continued). Chemical compositions of the Itokawa grains determined using the Cameca ims-5f ion microprobe.

Target	Grain C		Grain C		Grain C		Grain C	
Spot	7		8		9		10	
Phase	Di		Di		Pl*		$Pl_{0.95}Di_{0.05}$	
SiO_2	*54.08*		*54.08*		*66.95*	§	*66.31*	§
TiO_2	6,000	(140)	5,800	(270)	490	(17)	• • •	
Al_2O_3	5,700	(34)	7,600	(54)	200,000	(540)	• • •	
Cr_2O_3	9,000	(78)	9,000	(56)	-		• • •	
FeO	• • •		• • •		• • •		• • •	
NiO	-		310	(160)	-		• • •	
MnO	2,800	(25)	2,700	(29)	-		• • •	
MgO	• • •		• • •		• • •		• • •	
CaO	270,000	(1600)	260,000	(1800)	18,000	(160)	• • •	
Na_2O	7,100	(50)	5,800	(13)	68,000	(820)	• • •	
K_2O	10	(1)	12	(1)	7,700	(20)	• • •	
P_2O_5	-		-		340		310	(12)
H_2O	830	(23)	620	(18)	250	(9)	• • •	
Li†	-		-		• • •		• • •	
Li‡	0.27	(0.01)	0.22	(0.02)	0.04	(0.001)	• • •	
B	-		-		-		• • •	
F	8.6	(0.4)	11	(1)	160	(19)	330	(28)
Cl	-		5.9	(0.5)	44	(7)	8.7	(0.8)
Sr	8.3	(0.5)	11	(0.3)	73	(10)	• • •	
Y	12	(0.3)	12	(0.1)	0.09	(0.03)	• • •	
Zr	96	(1)	91	(0.4)	0.86	(0.02)	• • •	
Nb	1.1	(0.1)	1.1	(0.1)	0.28	(0.08)	• • •	
Ba	-		1.8	(0.2)	23	(2)	• • •	
La	-		0.62	(0.06)	0.54	(0.19)	• • •	
Ce	1.2	(0.1)	1.7	(0.1)	4.3	(2.5)	• • •	
Pr	-		0.29	(0.03)	0.87	(0.67)	• • •	
Nd	-		1.9	(0.1)	-		• • •	
Sm	-		0.93	(0.15)	0.64	(0.005)	• • •	
Eu	-		0.13	(0.02)	0.59	(0.12)	• • •	
Gd	-		1.1	(0.4)	0.50	(0.28)	• • •	
Dy	-		1.7	(0.1)	0.72	(0.30)	• • •	
Er	-		1.4	(0.2)	1.8	(0.2)	• • •	
Yb	-		1.5	(0.1)	1.8	(0.3)	• • •	
Lu	-		0.21	(0.05)	0.10	(0.01)	• • •	
Hf	-		3.5	(0.4)	2.0	(0.2)	• • •	

Table S7 (continued). Chemical compositions of the Itokawa grains determined using the Cameca ims-5f ion microprobe.

Target	Grain D		Grain D		Grain D	
Spot	11		12		13	
Phase	low-Ca Px		low-Ca Px		low-Ca Px	
SiO_2	*56.76*		*56.76*		*56.76*	
TiO_2	1,700	(62)	• • •		• • •	
Al_2O_3	2,300	(62)	• • •		• • •	
Cr_2O_3	920	(27)	• • •		• • •	
FeO	• • •		• • •		• • •	
NiO	-		• • •		• • •	
MnO	5,100	(29)	• • •		• • •	
MgO	• • •		• • •		• • •	
CaO	6,400	(120)	• • •		• • •	
Na_2O	110	(1)	• • •		• • •	
K_2O	-		• • •		• • •	
P_2O_5	-		-		• • •	
H_2O	330	(8)	• • •		• • •	
Li†	• • •		• • •		• • •	
Li‡	0.07	(0.01)	• • •		0.07	(0.01)
B	-		• • •		• • •	
F	8.9	(0.3)	12	(0.42)	• • •	
Cl	-		6.6	(0.26)	• • •	
Sr	0.10	(0.01)	• • •		-	
Y	0.34	(0.02)	• • •		0.36	(0.06)
Zr	0.32	(0.02)	• • •		-	
Nb	0.17	(0.04)	• • •		0.94	(0.22)
Ba	-		• • •		-	
La	-		• • •		-	
Ce	-		• • •		-	
Pr	-		• • •		-	
Nd	-		• • •		-	
Sm	-		• • •		-	
Eu	-		• • •		-	
Gd	-		• • •		-	
Dy	-		• • •		-	
Er	-		• • •		-	
Yb	-		• • •		-	
Lu	-		• • •		-	
Hf	-		• • •		-	

Table S8. Measured isotopes, possible interferences, and mass resolution power ($m/\Delta m$) to resolve each other in ion microprobe analyses of minerals mounted in In pools.

Target		Interference		$m/\Delta m$
$^{137}Ba^{+}$	136.906	$^{113}In^{24}Mg^{+}$	136.889	8,053
$^{139}La^{+}$	138.906	$^{115}In^{24}Mg^{+}$	138.889	8,171
$^{140}Ce^{+}$	139.905	$^{115}In^{25}Mg^{+}$	139.890	9,327
		$^{113}In^{27}Al^{+}$	139.886	7,363
$^{141}Pr^{+}$	140.908	$^{115}In^{26}Mg^{+}$	140.887	6,710
$^{147}Sm^{+}$	146.915	$^{115}In^{16}O_2^{+}$	146.894	6,996
$^{151}Eu^{+}$	150.920	$^{135}Ba^{16}O^{+}$	150.901	7,902
$^{157}Gd^{+}$	156.924	$^{141}Pr^{16}O^{+}$	156.903	7,473
		$^{115}In^{26}Mg^{16}O^{+}$	156.882	3,736
$^{163}Dy^{+}$	162.929	$^{115}In^{16}O_3^{+}$	162.889	4,073
		$^{115}In^{24}Mg_2^{+}$	162.874	2,962
		$^{147}Sm^{16}O^{+}$	162.910	8,575
$^{167}Er^{+}$	166.932	$^{115}In^{24}Mg^{28}Si^{+}$	166.866	2,529
		$^{151}Eu^{16}O^{+}$	166.915	9,705
		$^{135}Ba^{16}O_2^{+}$	166.896	4,599
$^{174}Yb^{+}$	173.939	$^{158}Gd^{16}O^{+}$	173.919	8,697
$^{175}Lu^{+}$	174.941	$^{159}Tb^{16}O^{+}$	174.920	8,331
$^{178}Hf^{+}$	177.943	$^{162}Dy^{16}O^{+}$	177.921	7,944

Table S9. Representative major element compositions of the merrillite in the PIC. Chemical compositions (in wt.%) were determined by FE-SEM with EDS, and normalized to 100 wt.% total. Abundances lower than the limits of detection (0.2 wt.%) are indicated by dashes.

Analytical No. (E004-)	pos24-8	pos24-9	pos22-5	pos22-6	pos23-7	pos45deg50T-2	pos0deg0t-1-2	AG-1-1
SiO_2	-	-	-	2.96	-	-	1.93	6.63
TiO_2	0.41	-	-	-	0.62	-	0.39	-
Al_2O_3	0.21	0.52	-	-	-	-	-	-
Cr_2O_3	-	1.51	-	1.42	0.86	0.53	0.42	-
FeO	-	0.83	0.23	9.30	1.44	0.71	0.44	-
NiO	-	-	-	0.68	-	2.60	-	-
MnO	1.66	0.61	-	-	0.81	-	0.88	1.30
MgO	3.35	3.07	3.72	3.84	3.64	3.09	4.02	6.06
CaO	46.33	47.57	46.32	43.46	45.17	46.15	47.43	42.95
Na_2O	2.44	2.14	3.12	0.35	2.36	1.86	-	-
K_2O	-	0.35	-	-	-	-	-	-

Table S10. Modal abundances of adhered objects (n=914). Volume was calculated assuming spheroidal shapes.

Phase	Volume (μm^3)	Modal abundance (%)
olivine	209.1	27.9
low-Ca pyroxene	148.7	19.8
plagioclase	104.7	14.0
diopside	25.5	3.4
K-feldspar	8.2	1.1
glass	162.5	21.7
Ca-phosphates	61.6	8.2
sulfide	18.8	2.5
spinel	10.7	1.4
total	749.8	100

SI Figures

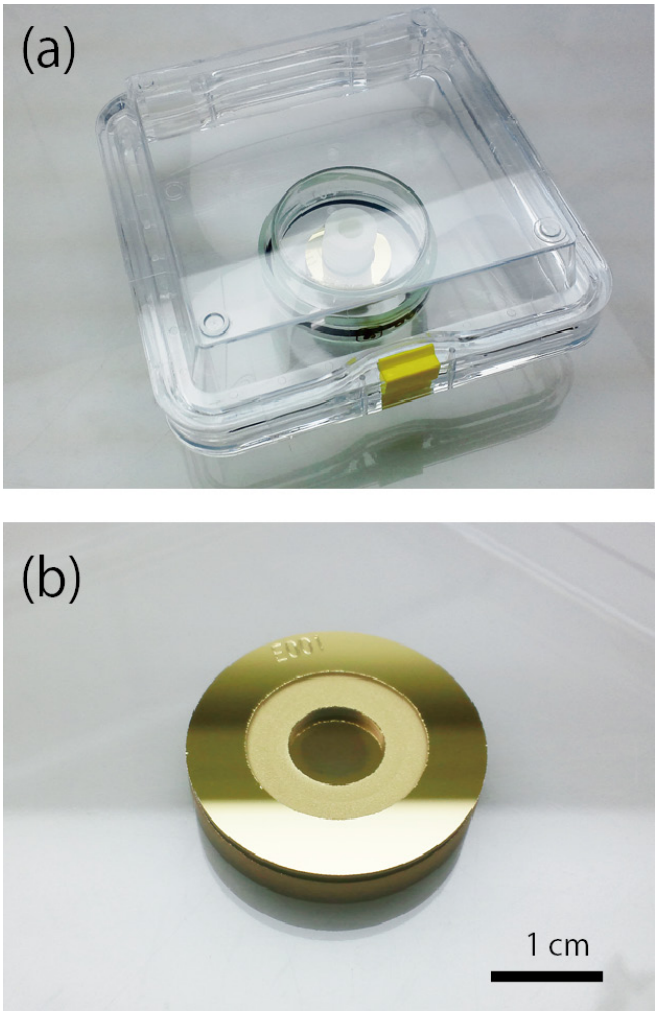

Fig. S1. Photos of the case to transport each grain from JAXA to PML. (a) A transport case assembly. The inner shell is suspended by a pair of membranes of the outermost shell. The container and its lid are fixed by a plastic spring in the inner shell. (b) The sample container with Au coating. The sample grain is stored at the bottom of the pit and the lid fits tightly with the frosted area.

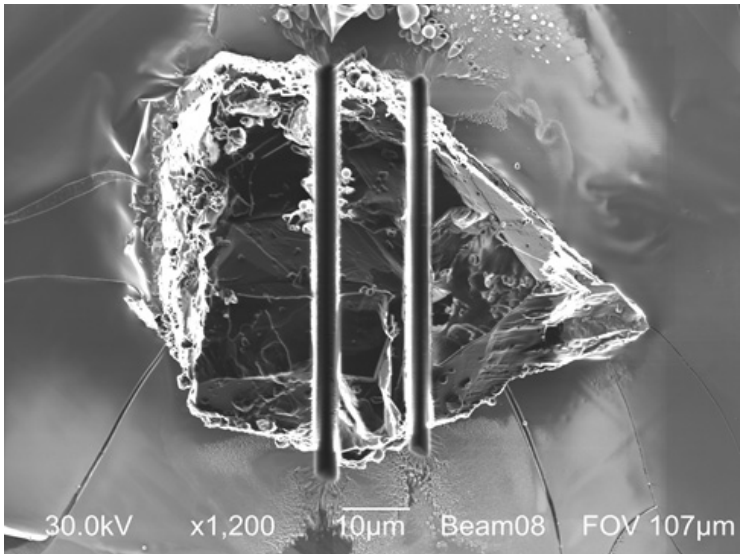

Fig. S2. A scanning ion image of Grain C fabricated into three pieces. Sample loss with the slicing was typically a ~3μm wide zone. Re-deposition of gallium was observed on the edge of surfaces produced by the slicing. A middle slab, which is ~12 μm in thick, was processed for quantitative in-situ analyses. Maintaining the possibility of future analyses is as important as the initial analyses and other two slices were preserved for possible future investigation.

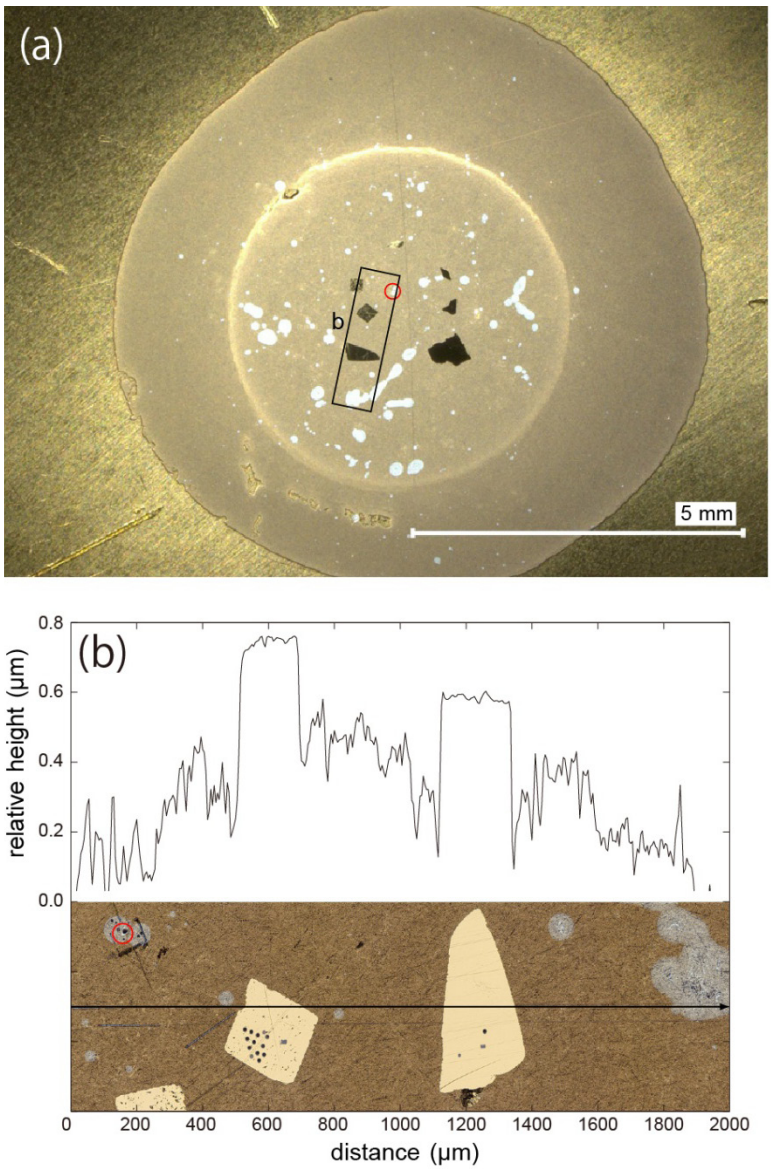

Fig. S3. The surface of the sample mount. (a) Reflected-light image of an In-pool containing the slab of Grain A (red circle) and 6 reference materials. (b) Surface-height profile across 2,000-μm traverse, the location of which is indicated as the rectangular area "b" in Fig. S3a.

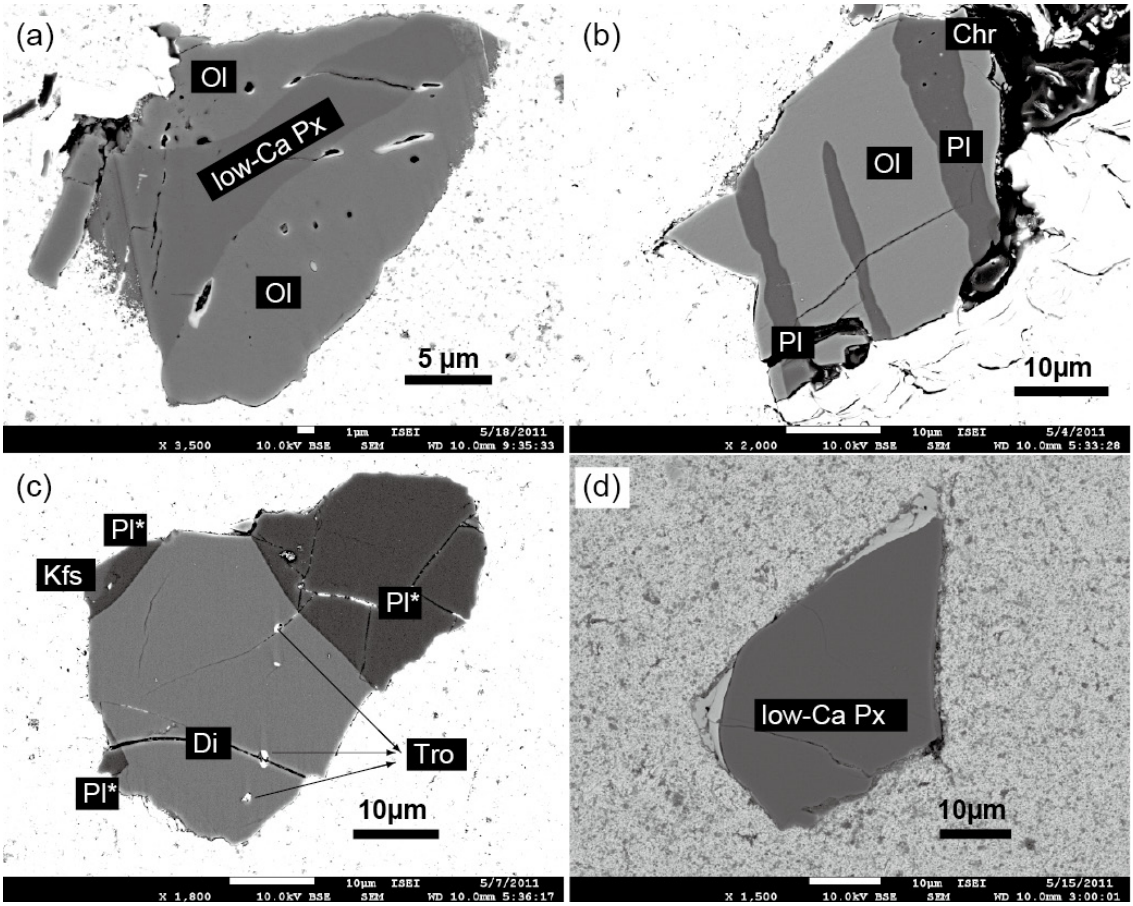

Fig. S4. Back-scattered electron images of the slabs of (a) Grain A, (b) Grain B, (c) Grain C, and (d) Grain D. Abbreviations Ol, low-Ca Px, Pl, Pl*, Chr, Di, Kfs, and Tro denote olivine, low-Ca pyroxine, plagioclase, diaplectic plagioclase, chromite, diopside, K-feldspar, and troilite, respectively.

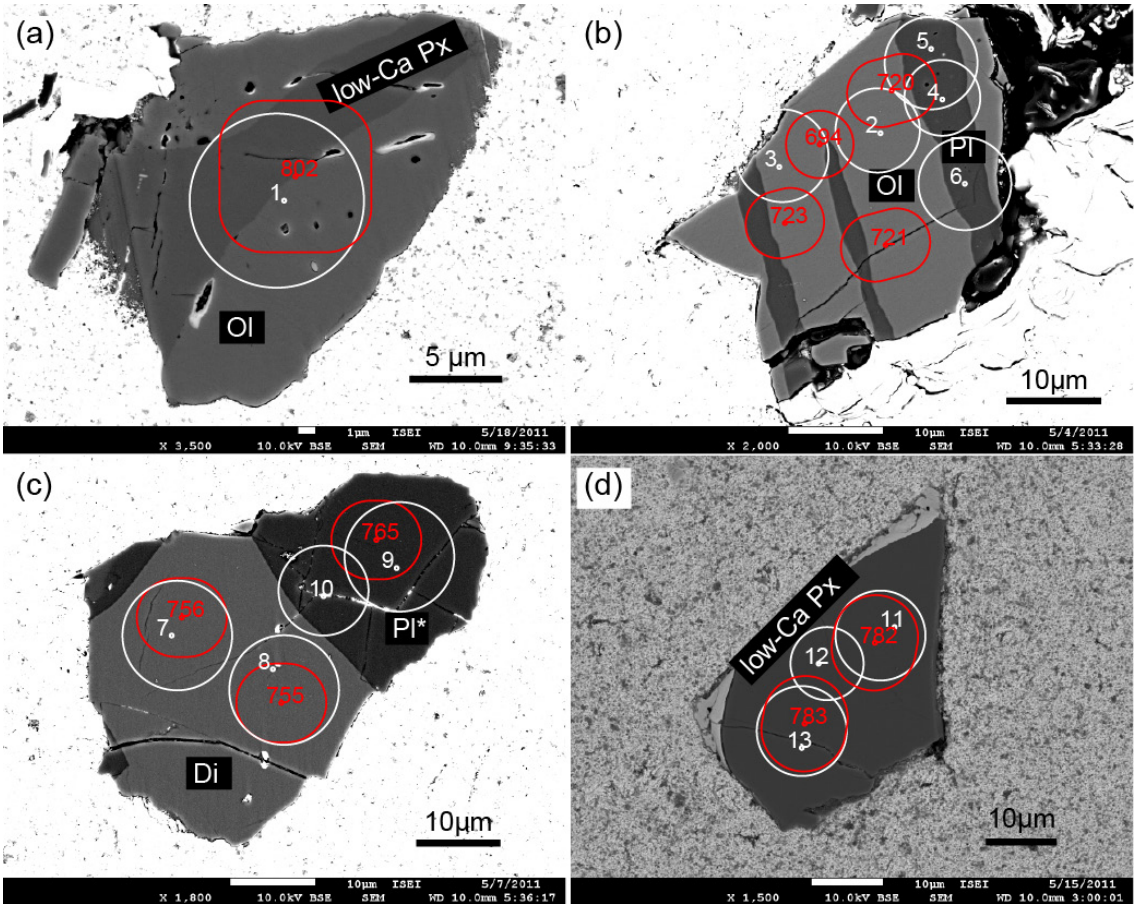

Fig. S5. Back-scattered electron images showing sites analyzed by the ion microprobes on slabs of (a) Grain A, (b) Grain B, (c) Grain C, and (d) Grain D. Red ovals and white circles show the locations of areas analyzed for oxygen isotopes (ims-1270) and elemental abundances (ims-5f), respectively. Numbers in the ovals and circles correspond to the spot numbers given in Tables S3 and S7.

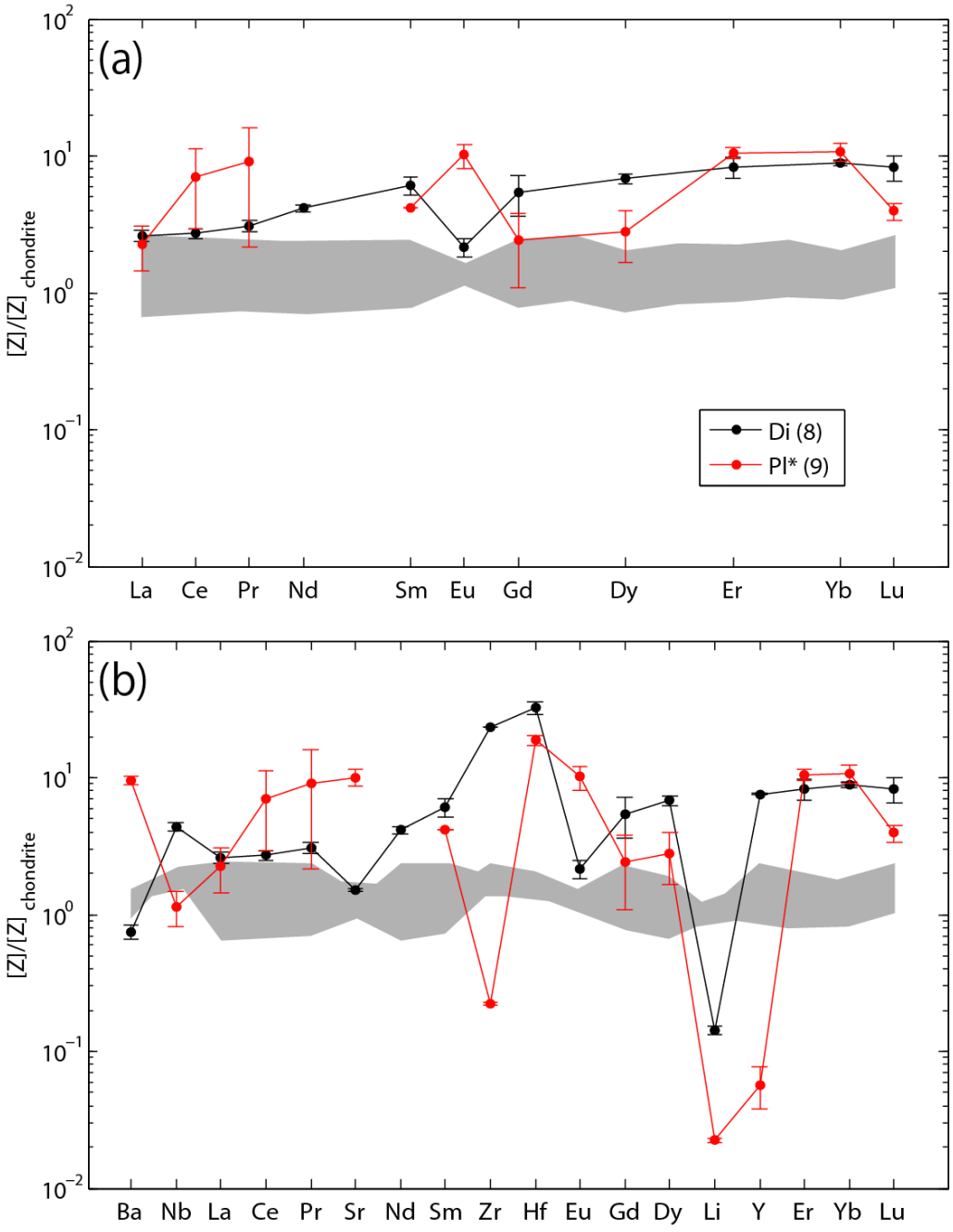

Fig. S6. Chondrite-normalized element abundances for diopside (Di) and diaplectic plagioclase (Pl*) in Grain C. Numbers in the parentheses correspond to the spot numbers given in Table S7 and Fig. S5. Shaded fields show ranges for L4–6 and LL4–6 bulk chondrites.[46,47] Element abundances for chondrite are after Anders and Grevesse (1989).[48] (a) The diopside exhibits a slightly light-REE-depleted pattern with a negative Eu anomaly, and the diaplectic plagioclase shows a flat pattern with a positive Eu anomaly. (b) The Li-depleted patterns for diopside and diaplectic plagioclase in Grain C are perhaps indicative of later aqueous alteration processes.

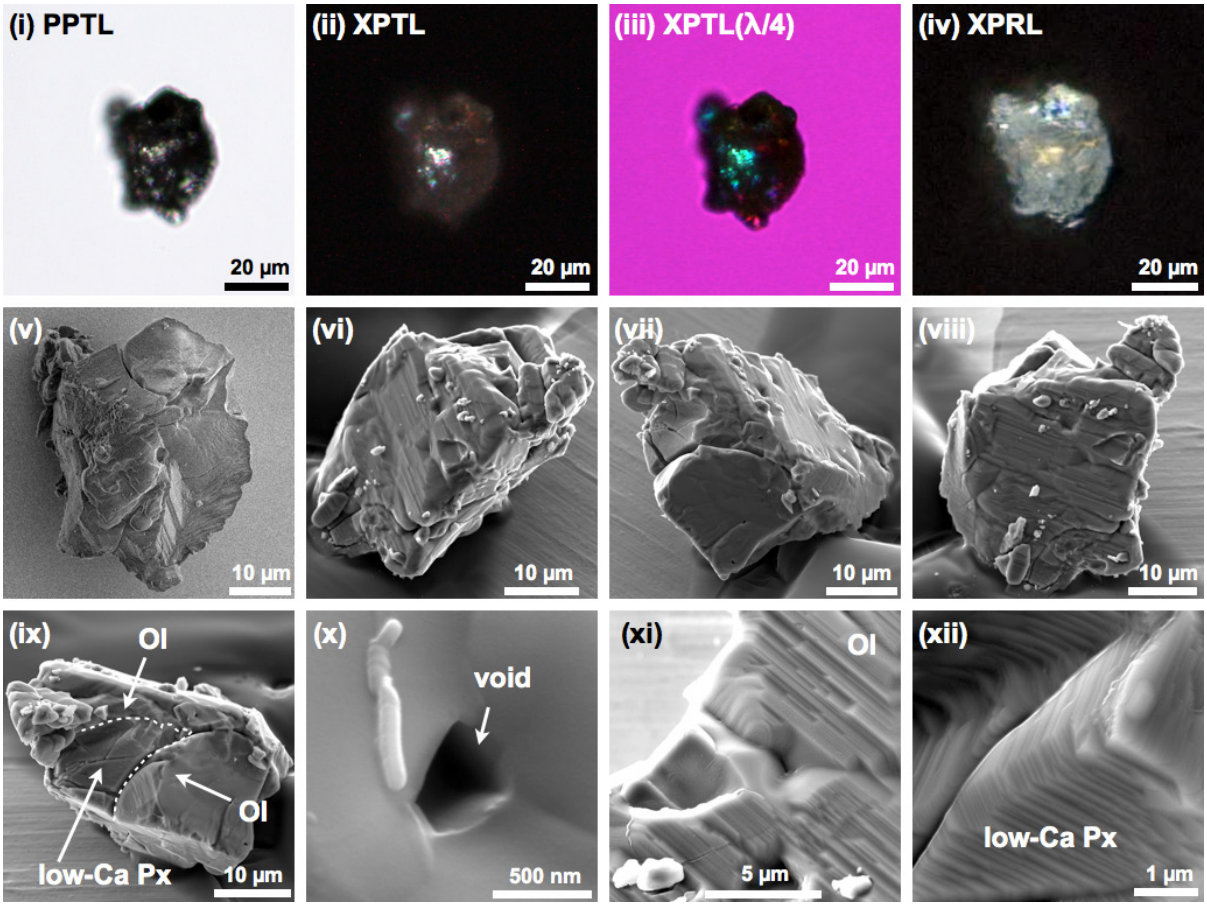

Fig. S7a. Micrographs of Grain A showing an appearance indicative of extensive shock-induced deformation and fracturing. (i) Plane-polarized transmitted light (PPTL) view. (ii) Cross-polarized transmitted light (XPTL) view of (i). The optical appearance of this grain indicates that it is a polyphase grain. The olivine (Ol) shows reduced transparency due to the presence of shock lamellae. (iii) XPTL view of (i) with a quarter-wavelength plate inserted into the petrographic microscope. (iv) Cross-polarized reflected light (XPRL) view. (v) Secondary electron (SE) image taken at low acceleration voltage without C coating. (vi), (vii), (viii) and (ix) Grain appearances at different angles. All of these images were taken after C coating. Strong shock deformation is evident from the presence of shock lamellae in olivine and deep fractures (cracks). (x) Close-up view of a smooth surface on low-Ca pyroxene (low-Ca Px) with a void possibly reflecting troilite desulfidization (vaporization). (xi) Close-up view of a typical surface of olivine with shock lamellae. (xii) Close-up view of a surface of low-Ca pyroxene with prominent cleavage.

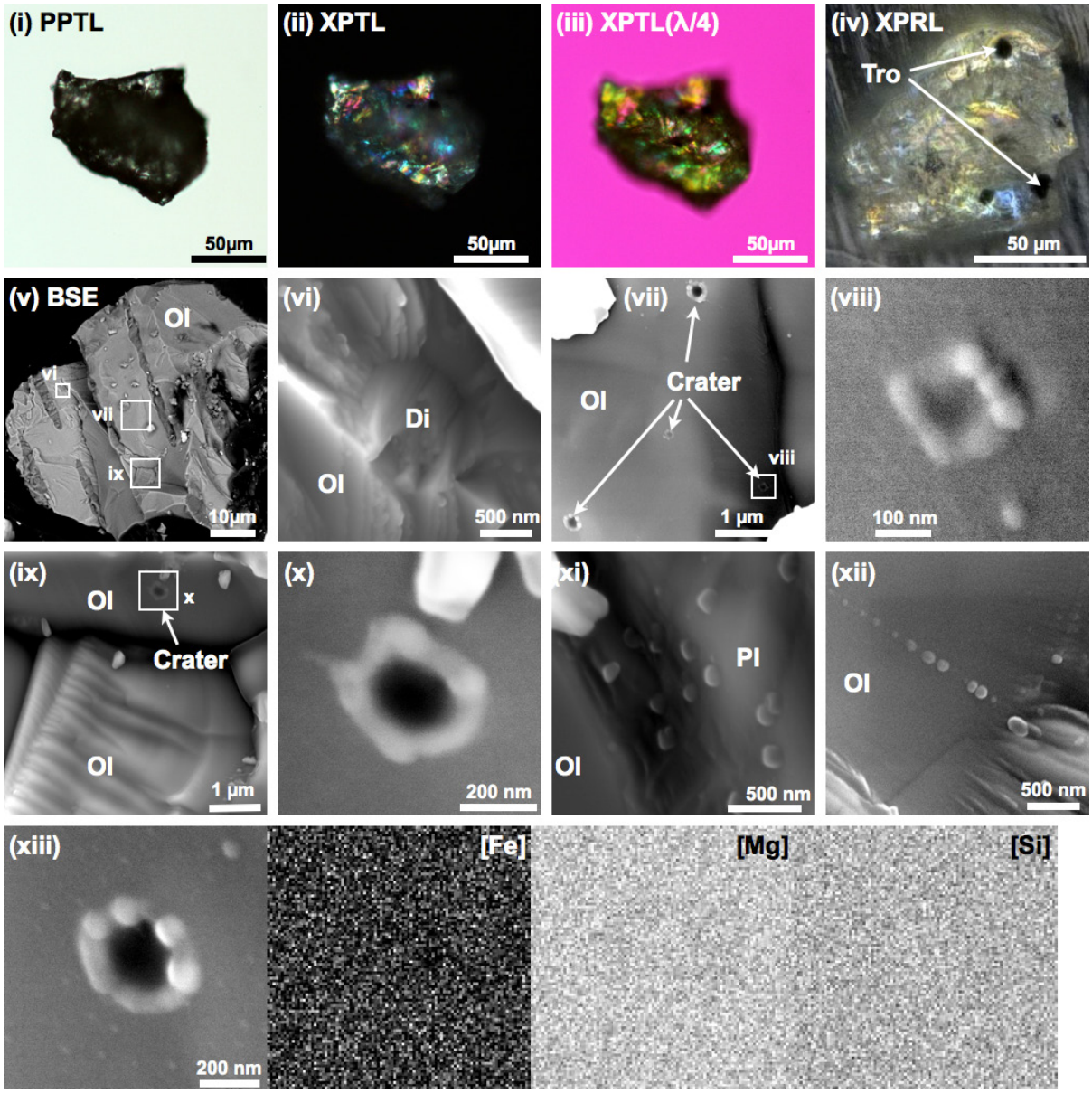

Fig. S7b. Micrographs of Grain B that preserves submicron-sized impact texture. (i) PPTL view. (ii) XPTL view of (i). The grain is an optically continuous single crystal. (iii) XPTL view of (i) with a quarter-wavelength plate inserted. (iv) XPRL view. Opaque minerals are troilite. (v) Back-scattered electron (BSE) image. The sub-parallel intergrowth of plagioclase within mono-phase olivine, which resembles the barred olivine texture in some chondrules, is believed to reflect original lithology. (vi) Occurrence of a diopside (Di) inclusion in olivine. (vii) A smooth olivine surface with a cluster of four sub-μm-sized craters. (viii) Enlargement view of a crater in (vii). Other similar images are presented in Fig. 2. (ix) Occurrence of a crater on smooth surface and a fracture plane with shallow, sub-parallel, linear fractures. (x) Enlargement view of a crater in (ix). (xi) Close-up view of a boundary between plagioclase and olivine. Nanometer-sized particles are adhered to plagioclase. (xii) Close-up view of nm-sized particles aligned on a fracture plane of olivine. (xiii) Submicron-sized crater (same as crater 3 of Fig. 2e) and X-ray maps (Fe, Mg, and Si) indicating the lack of obvious compositional differences between the host olivine and the crater rim.

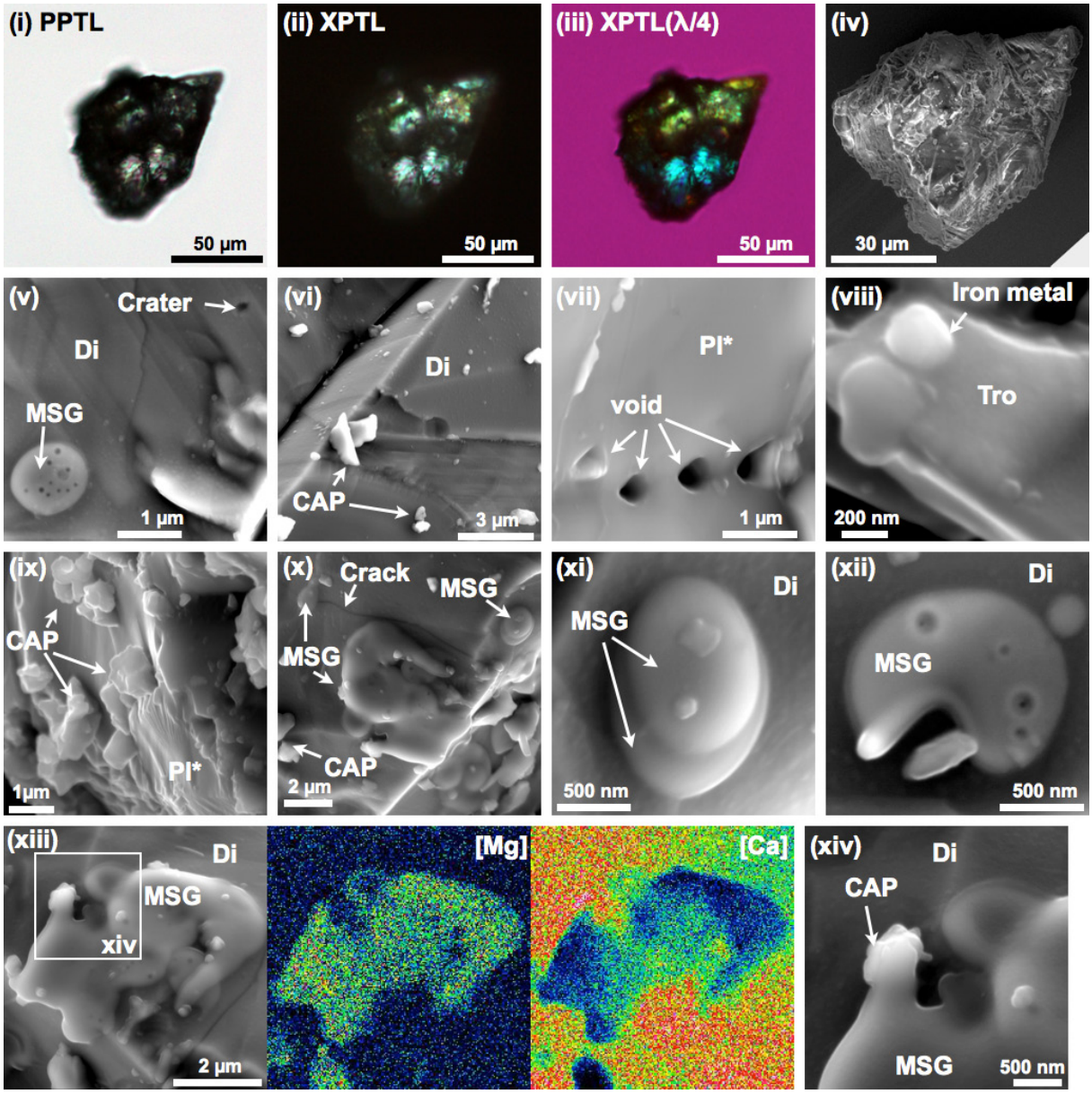

Fig. S7c. Micrographs of Grain C showing various surface features including adhered melts. (i) PPTL view. (ii) XPTL view of (i). (iii) XPTL view of (i) with a quarter-wavelength plate inserted. The optical appearance of this grain indicates that it is a polyphase grain. (iv) SE image taken at low- acceleration voltage without C coating. Note that Fig. 3a shows the reverse side of the same grain. (v) Facture plane of diopside (Di) with sub-µm-sized crater (Fig. 3d) and molten splash-shape glass (MSG) (Fig. 3h). (vi) Fracture plane in diopside with common adhered particles (CAPs). (vii) Voids produced by troilite desulfidization (vaporization) on surface of diaplectic plagioclase (Pl*). This is a different angle of view of the voids from that shown in Fig. 3c. (viii) Occurrence of Fe metal on troilite (Tro). The coexistence of Fe metal and troilite might indicate high-T desulfidization by thermal metamorphism. The Fe metal formation due to desulfidization is explained by an increase in temperature at a constant S fugacity or by an isothermal decrease in the S fugacity. (ix) Grain wall with abundant CAPs. Some olivine CAPs exhibit flaky shapes. It is likely that the flaky CAPs originated in highly deformed crystals. (x) Adhered MSGs and CAPs on diopside. The presence of a MSG on a microcrack indicates adhesion after the brittle fracturing events. (xi) Two flattened disk-shaped MSGs lying upon each another. (xii) MSG with vesicles believed to reflect degassing. (xiii) An irregularly-shaped MSG (MSG1 of Fig. 3g) and its X-ray (Mg and Ca) images. The object has low SiO_2 (38.5 wt%), high MgO (24.6 wt%), FeO (23.8 wt%), and low CaO (9.6 wt%) and is compositionally different from substrate diopside. (xiv) Enlarged view of CAP associated with the MSG also shown in (xiii).

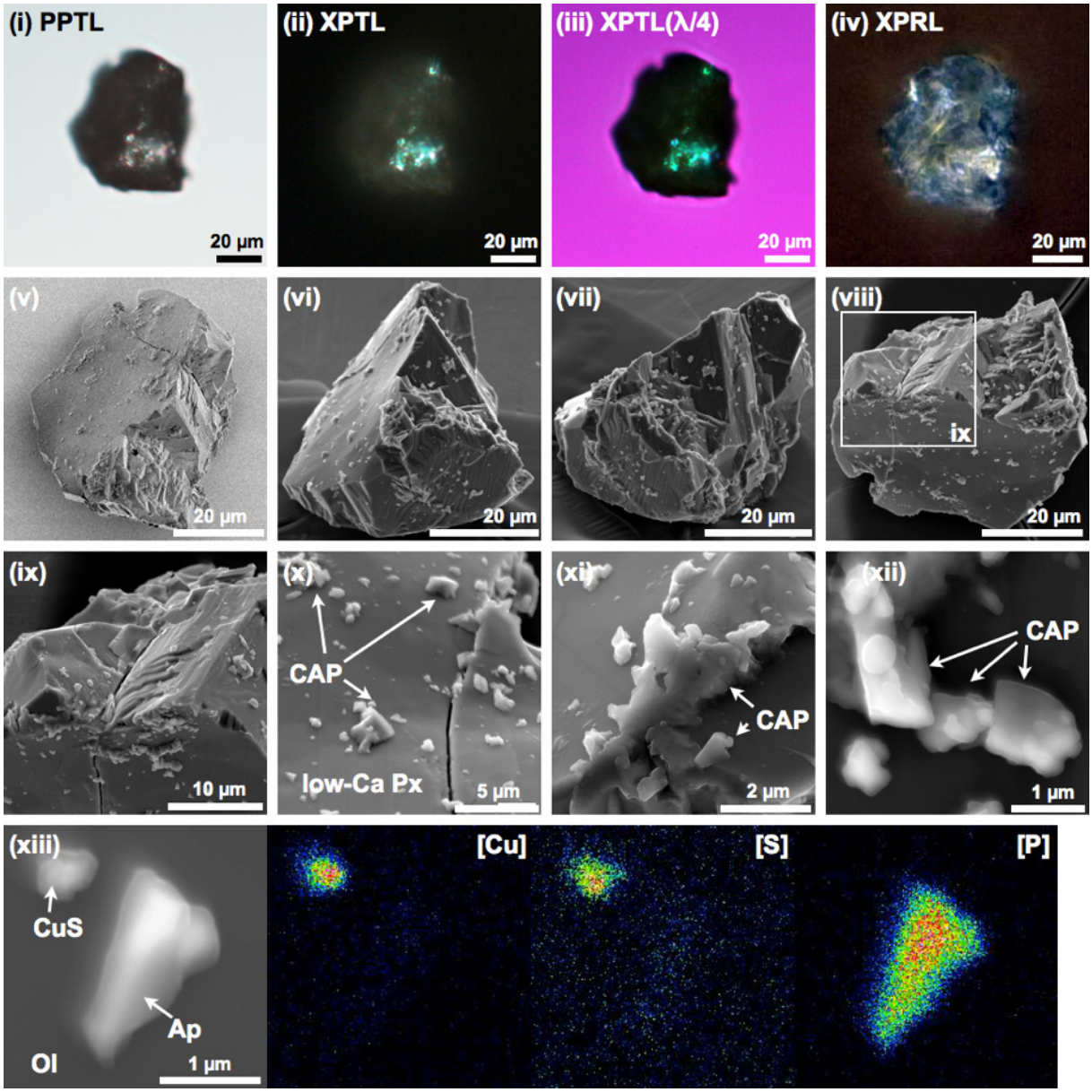

Fig. 7d. Micrographs of Grain D showing abundant adhered objects on grain periphery. (i) PPTL view. (ii) XPTL view of (i). (iii) XPTL view of (i) with a quarter-wavelength plate inserted. (iv) XPRL view. The optical appearance of this grain indicates that it is a polyphase grain. (v) SE image taken at low acceleration voltage without C coating. (vi), (vii), and (viii) Grain appearances in different angles. All of these images were taken after C coating. The grain morphology is characterized by a smooth fracture plane with very rough surfaces. The smooth fracture plane is partially cracked. (ix) Enlarged view of a rough fracture plane with sub-parallel linear fractures shown in (viii). The sub-parallel linear structures are likely related to the cleavage. (x) Occurrence of CAPs on the smooth fracture plane. (xi) Adhered CAPs at the edge of a fracture plane. (xii) Close-up view of a composite CAP. (xiii) Occurrence of CuS as a common adhered particle (CAP) on an olivine surface, and X-ray images of the same area for Cu, S, and P. The larger CAP in this area is Cl-bearing apatite (Ap; see the X-ray image for P).

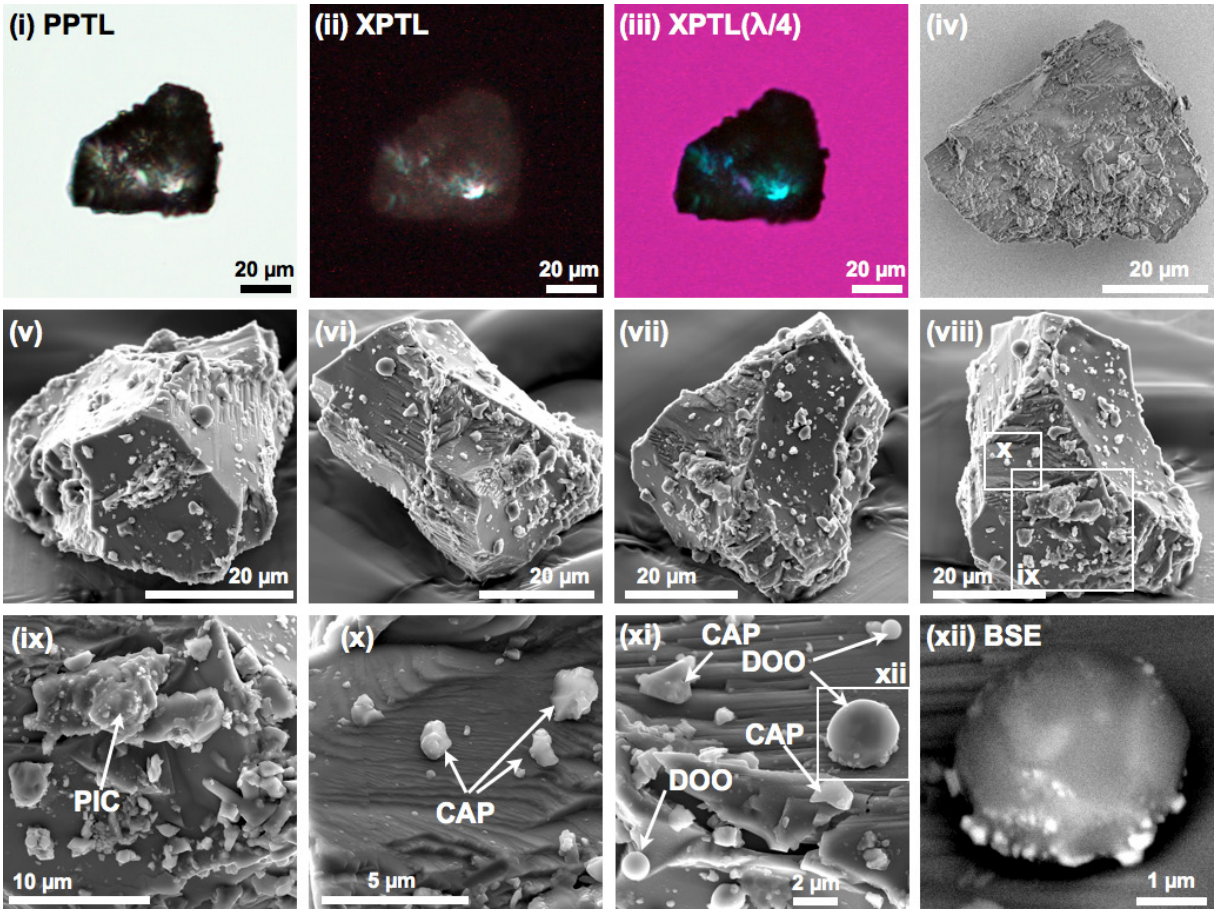

Fig. S7e. Micrographs of Grain E having peculiar adhered objects. (i) PPTL view. (ii) XPTL view of (i). (iii) XPTL view of (i) with a quarter-wavelength plate inserted. The optical appearance of this grain indicates that it is a monophase grain. (iv) SE image taken at low acceleration voltage without C coating. (v), (vi), (vii), and (viii) Grain appearances from different angles. The grain has at least five fracture planes. All of these images were taken after C coating. (ix) Enlarged view of particularly irregularly-shaped clot (PIC). See the more detailed explanation in Fig. S8. (x) Enlarged view of fracture plane in (viii). The sub-parallel linear structures are likely related to the cleavage. (xi) Occurrence of dome-outline object (DOO). (xii) BSE image of DOO in Fig. 4b.

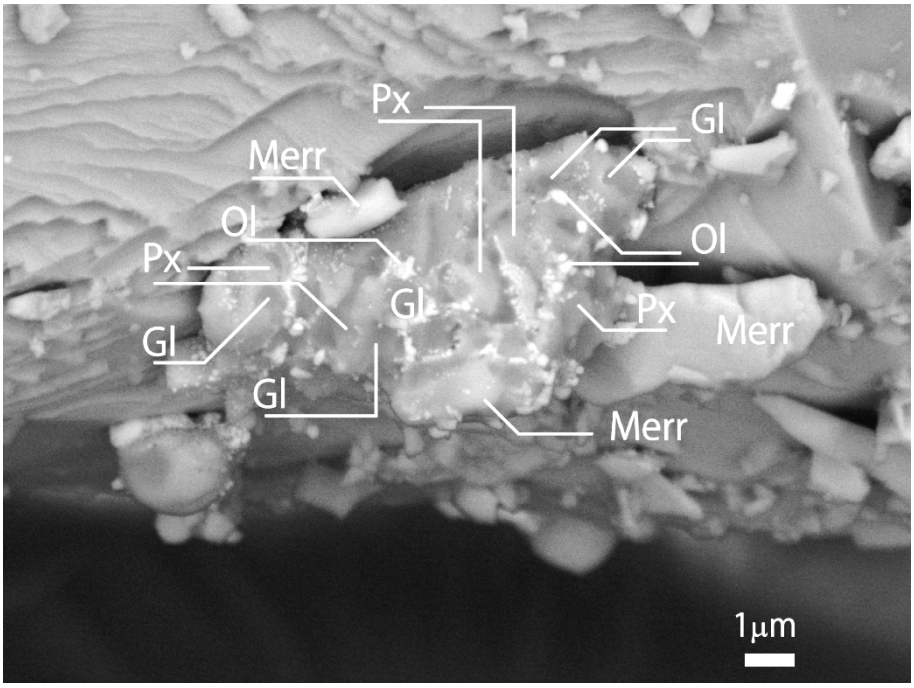

Fig. S8. Back-scattered electron image of the PIC. The PIC consists of merrillite (Merr), olivine (Ol), low-Ca pyroxene (Px), and glass (Gl). Petrographic observations suggest that PICs are fragments of quenched melt pool, features commonly associated with shock-induced veins in ordinary chondrites.

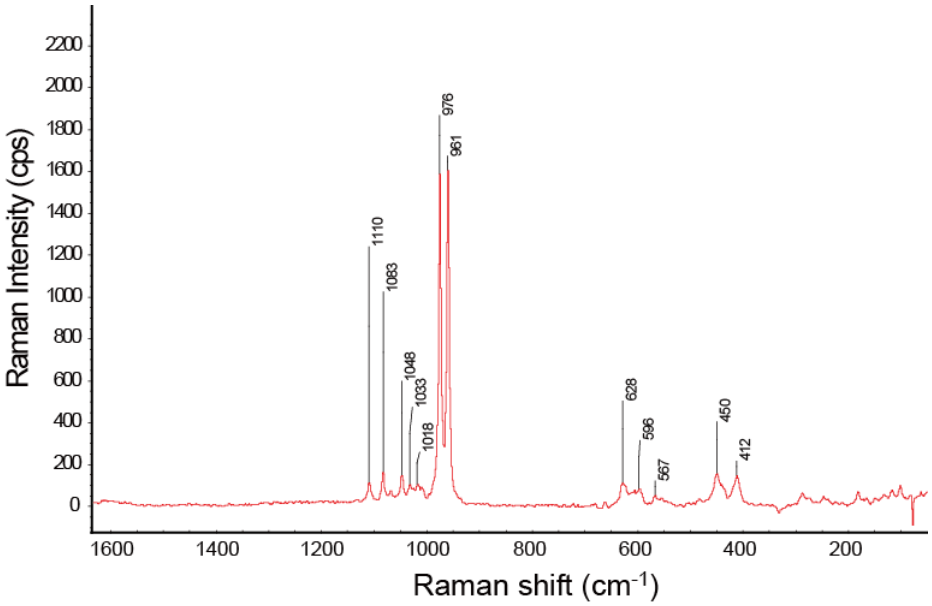

Fig. S9. Raman spectrum of merrillite in the PIC. Remarkable absorptions at 961 and 976 cm^{-1} correspond to the v_1 symmetric stretching mode of PO_4^{3-} ions. Also observed are representative bands at 1083, 450, and 412 cm^{-1}.

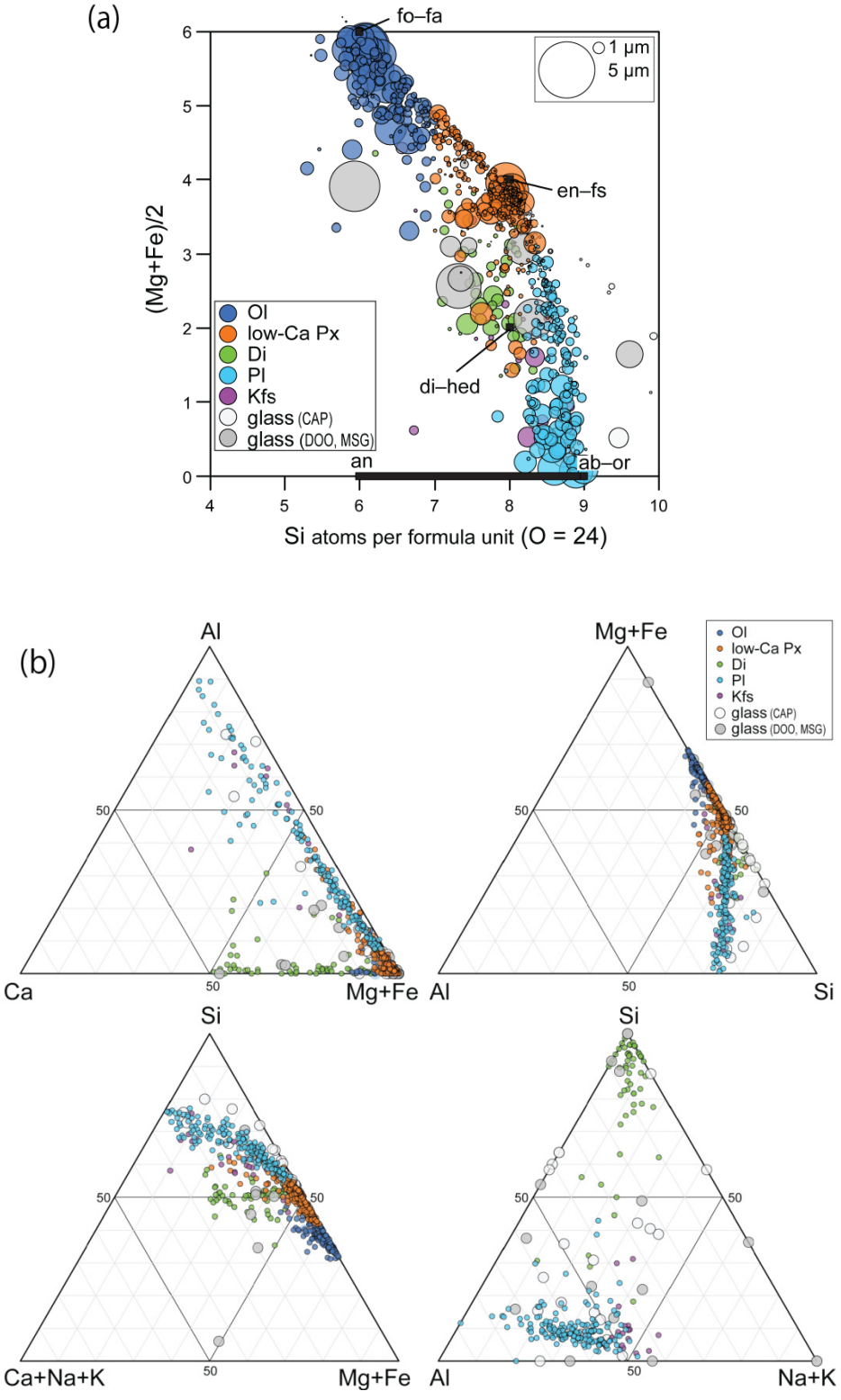

Fig. S10. Apparent chemical compositions of adhered objects. Properties of adhered objects, including compositions and sizes, are listed in SI Data. (a) Apparent compositions obtained for 914 adhered objects. Mean object sizes are represented by the circle sizes. Apparent variation is explained as mixing between a target and the substrate mineral. Some glasses plot off of the expected mixing lines. (b) Apparent compositions on ternary diagrams.

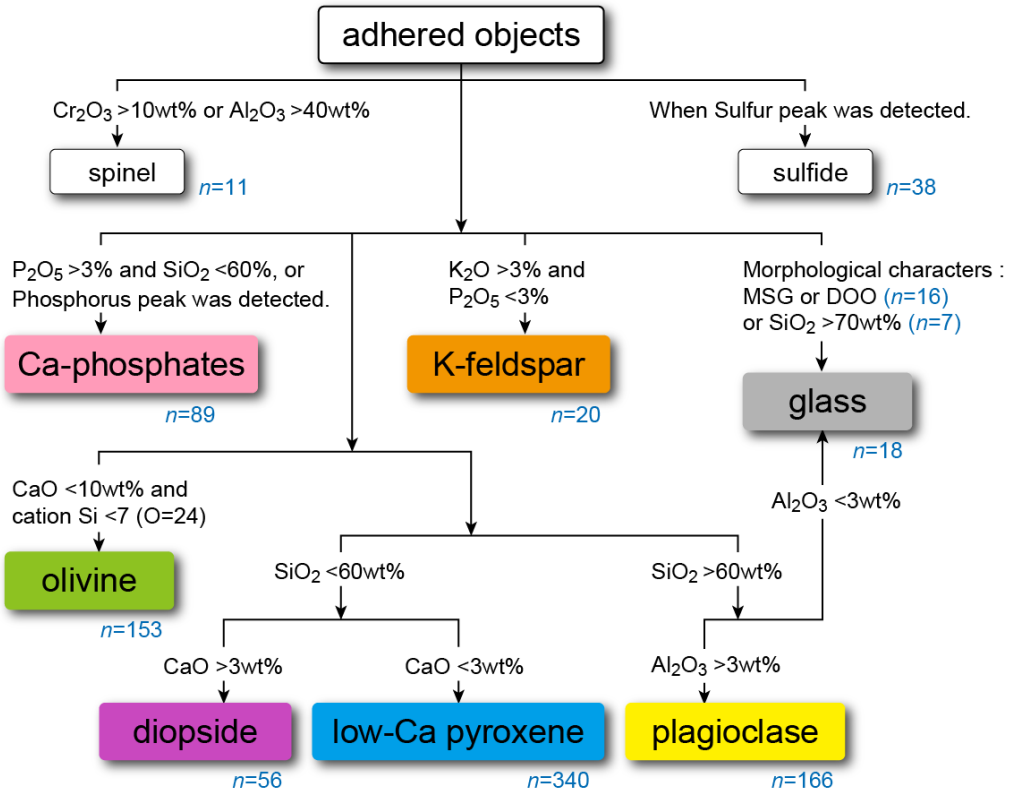

Fig. S11. A Flow chart for identification of the phases in the adhered objects. Whether a phase is Ca-phosphate or K-feldspar is deduced by examination of the elemental abundances of P_2O_5 and K_2O. If an object can be morphologically categorized as being a MSG or DOO, or its abundant of SiO_2 is higher than 70 wt.%, it is identified as glass. Remaining phases are assigned as being olivine, plagioclase, diopside, or low-Ca pyroxene. Note that plagioclase with Al_2O_3 abundance lower than 3 wt.% is re-categorized to glass. Number of objects in each category is shown below the colored boxes.